Università degli Studi di Padova

Dipartimento di Fisica e Astronomia "Galileo Galilei"
Master Degree in Physics

Final Dissertation

Peripheral lung cancers treated with photon, proton, and carbon ion beams: comparative study of dose distribution, robustness, and NTCP analysis

Thesis Supervisor
Prof. Laura De Nardo

Thesis Co-Supervisors
Dr. Luca Trombetta

Candidate
Carlotta Lizzi

Matriculation Number
1236667

Academic Year 2024-2025

To my mother,
a lighthouse in every storm

"Nothing in life is to be feared, it is only to be understood.
Now is the time to understand more, so that we may fear less."

— Marie Curie

Contents

List of abbreviations

RT	Radiotherapy
IR	Ionizing radiation
EBRT	External Beam Radiotherapy
IMRT	Intensity-Modulated Radiotherapy
SRT	Stereotactic Radiotherapy
HT	Hadron Therapy
CSDA	Continuous Slowing Down Approximation
MCS	Multiple Coulomb Scattering
RBE	Relative Biological Effectiveness
SOBP	Spread Out Bragg Peak
WEPL	Water-Equivalent Path Length
HU	Hounsfield Units
ROI	Region of Interest
LET	Linear Energy Transfer
SSBs	Single-Strand Breaks
DSBs	Double-Strand Breaks
PE	Plating Efficiency
LQ	Linear-Quadratic
EQD2	Equivalent Dose in 2 Gy Fractions
BED	Biologically Effective Dose
LEM	Local Effect Model
CNAO	National Center for Oncological Hadrontherapy
IGRT	Image-Guided Radiotherapy
CT	Computed Tomography
OARs	Organs at Risk
TPS	Treatment Planning System
GTV	Gross Tumor Volume
CTV	Clinical Target Volume
ITV	Internal Target Volume
PTV	Planning Target Volume
TV	Treatment Volume
IV	Irradiated Volume
DVH	Dose-Volume Histograms
SBRT	Stereotactic Body Radiotherapy

4D-CT	Four-Dimensional Computed Tomography
IRCCS	Istituti di Ricovero e Cura a Carattere Scientifico
VMAT	Volumetric-Modulated Arc Therapy
FFF	Flattening Filter Free
MLC	Multi-Leaf Collimator
IMPT	Intensity-Modulated Proton Therapy
MFO	Multifield Optimization
HI	Homogeneity Index
CI	Conformity Index
GI	Gradient Index
IQR	Interquartile Range
CIRT	Carbon Ion Radiotherapy
SD	Standard deviation
NTCP	Normal Tissue Complication Probability
LKB	Lyman-Kutcher-Burman
EUD	Equivalent Uniform Dose
RP	Radiation-induced pneumonitis
RF	Rib fractures
MLD	Mean lung dose
3D-CRT	Three-Dimensional Conformal Radiation Therapy

Introduction

The field of nuclear physics has played a pivotal role in advancing oncological research, providing essential tools for both diagnosis and treatment of cancer. From the discovery of radiation and its biological effects to the development of nuclear imaging and radiotherapy techniques, the application of fundamental physics to medicine has continuously evolved. Conventional radiotherapy, which predominantly uses high-energy X-rays, has long been a cornerstone in cancer treatment. While effective, photon-based therapies often involve irradiation of healthy tissues surrounding the tumor, potentially leading to side effects and limiting dose escalation.
One of the most advanced applications of nuclear physics in oncology is hadron therapy, a highly precise form of radiotherapy that exploits charged particle beams, such as protons and carbon ions, to target tumors with high accuracy. The physical foundation of hadron therapy is based on the Bragg peak phenomenon, a characteristic energy deposition pattern exhibited by charged particles. Unlike photons, employed in conventional radiotherapy, protons and heavy ions deposit most of their energy in a well-defined depth, corresponding to the Bragg peak, after which the dose drops sharply. This property allows for a more localized and controlled dose distribution, minimizing damage to surrounding healthy tissues and improving the therapeutic ratio. In Italy, the National Center for Oncological Hadrontherapy (CNAO) in Pavia stands as a reference center in the field of particle therapy. Designed as a hub of excellence for the clinical application of proton and carbon ion therapy, CNAO is among the few facilities worldwide equipped with a synchrotron capable of accelerating charged particles to high energies. This technology enables the effective treatment of deep-seated and radioresistant tumors, offering a precise and highly localized dose delivery. In addition to its clinical role, CNAO serves as a research facility, contributing to the development of innovative treatment protocols and the exploration of new applications of charged particle therapy in oncology.
This thesis is set within this framework and aims to compare three advanced treatment techniques for lung stereotactic body radiation therapy (SBRT):

- Volumetric Modulated Arc Therapy (VMAT) with photons;
- Intensity-Modulated Proton Therapy (IMPT);
- Carbon ions Radiotherapy (CIRT).

The study was conducted using 20 4DCT datasets of peripherally located lung lesions. The IMPT and CIRT plans were optimized using a gated and robust approach at the Clinical Target Volume (CTV) level, incorporating systematic uncertainties, density variations,

and anatomical changes due to respiratory motion. In contrast, the VMAT plans were optimized based on a Planning Target Volume (PTV) derived from the Internal Target Volume (ITV), with gating on the maximum inhalation phase. The comparison among these treatment techniques was conducted in a multicenter setting, with VMAT plans optimized by the Medical Physics Unit at Fondazione IRCCS San Gerardo dei Tintori in Monza. The study analyzed key dosimetric parameters, including CTV coverage, organ-at-risk (OAR) sparing in terms of biologically effective dose (BED), conformity index, homogeneity index, gradient index, and plan robustness. Additionally, a radiobiological assessment was performed by calculating the Normal Tissue Complication Probability (NTCP) to evaluate the clinical impact of different treatment approaches. This study introduces several innovative aspects compared to existing literature. While previous research has compared proton and photon-based approaches for lung SBRT, no study has specifically investigated the use of IMPT with patient-specific collimators. Furthermore, the application of robust planning directly at the CTV level in proton therapy represents a novel approach in this type of dosimetric comparison. The structure of the thesis is as follows:

- Chapter 1: Introduces the fundamental principles governing the interaction of photons and charged particles with matter, covering both physical and radiobiological aspects essential for understanding treatment modalities;
- Chapter 2: Explains the key principles of treatment planning, detailing the methodologies followed in this study for constructing and optimizing treatment plans for the different radiation modalities;
- Chapter 3: Presents the design of the study, describing the dataset and outlining the characteristics of the three treatment techniques compared in this work;
- Chapter 4: Focuses on the evaluation and comparison of the treatment plans from multiple perspectives, including dosimetric analysis, robustness assessment, and radiobiological evaluation;
- Chapter 5: Summarizes the conclusions drawn from the study and discusses future perspectives.

Chapter 1

Interaction of Photons and Charged Particles with Matter: from Physical Principles to Radiobiology

Radiotherapy (RT) is a pillar of cancer treatment that employs ionizing radiation (IR) with energy levels sufficient to remove electrons from atoms or molecules within tissues, a mechanism used to damage and destroy malignant cells. In radiation therapy, one of the most critical parameters is the dose deposited by particles within tissues. The absorbed dose is defined as the average amount of energy deposited per unit mass in a medium as a result of exposure to ionizing radiation. This quantity is essential to evaluate the effectiveness and safety of the treatment, as it is directly correlated with the biological effects induced in the irradiated tissues.[1]

$$D = \frac{dE}{dm} \tag{1.1}$$

Radiotherapy is categorized into two primary forms: External Beam Radiotherapy (EBRT) and Internal Radiotherapy. EBRT, the most widely used form, involves delivering radiation from an external source, which directs focused beams toward the tumor site. Advanced EBRT techniques, such as Intensity-Modulated Radiotherapy (IMRT) and Stereotactic Radiotherapy (SRT), allow for precise dose distribution tailored to the tumor's complex geometry, thereby sparing adjacent healthy tissues. In contrast, Brachytherapy, a form of Internal Radiotherapy involves the placement of radioactive sources directly within or near the tumor, maximizing the localized dose to the tumor, while minimizing exposure to surrounding healthy tissue.
This study will primarily address EBRT, which traditionally utilizes photon beams, such as X-rays or gamma rays, to penetrate tissue and deliver energy along the tumor path.

[1] In the International System of Units (SI), the unit of measurement for absorbed dose is the Gray (Gy). One Gray is defined as the absorption of one joule of ionizing radiation energy per kilogram of matter.

However, Hadron Therapy (HT), a specialized form of radiotherapy, employs charged particles like protons or heavier ions, such as carbon. These particles offer distinct advantages due to their unique physical properties: unlike photons, which gradually deposit energy along their trajectory, charged particles release the majority of their energy at the end of their path giving rise to the so called Bragg peak. This peak enables highly targeted treatment of tumors, minimizing the impact on nearby healthy tissues and making HT particularly effective for deep-seated or radiation-resistant tumors.

1.1 Interaction of particles with matter

In order to fully understand the fundamental differences between conventional radiotherapy and hadron therapy, a deep knowledge of radiation interactions with matter is essential.

1.1.1 Photon interaction mechanism

Although numerous possible interaction mechanisms are known for photons in matter, only three principal types play a significant role for medical physics applications: photoelectric absorption, Compton scattering, and pair production, leading to the ejection of orbital electrons from atoms or the formation of electron-positron pairs. These liberated charged particles subsequently lose energy gradually leading to radiobiological effects.

1.1.1.0.1 Photoelectric absorption: In the process of photoelectric absorption, a photon interacts with an absorber atom, resulting in the complete absorption of the photon. Consequently, an energetic photoelectron is ejected from one of the atom's bound shells. For sufficiently high energy photons, the photoelectron is most likely to originate from the atom's most tightly bound shell, typically the K-shell. The energy of the emitted photoelectron is given by:

$$E_{e^-} = h\nu - E_b \tag{1.2}$$

Where E_b is the binding energy of the photoelectron within its original shell. For photon energies exceeding several hundred keV, the photoelectron retains the majority of the initial photon energy. In addition to the ejection of the photoelectron, the interaction also results in the formation of an ionized absorber atom with a vacancy in one of its bound shells. This vacancy is rapidly filled through the capture of a free electron from the surrounding medium and/or the rearrangement of electrons from other atomic shells. Consequently, one or more characteristic X-ray photons (or Auger electrons) may also be emitted. The photoelectric effect is the dominant mode of interaction for gamma rays (or X-rays) at relatively low energies. This process is further enhanced for absorber materials with a high atomic number (Z). Although no single analytical expression accurately represents the probability of photoelectric absorption per atom across all ranges of E_γ and Z, a rough approximation is:

$$\tau \simeq constant \cdot \frac{Z^n}{{E_\gamma}^{3.5}} \tag{1.3}$$

where the exponent n varies between 4 and 5 over the photon energy region of interest.

1.1.1.0.2 Compton scattering: The Compton scattering interaction occurs between an incident photon and an electron within the absorbing material. During Compton scattering, the incident photon is deflected at an angle θ relative to its original direction, transferring a portion of its energy to the electron, which is then referred to as a recoil electron. Since all scattering angles are possible, the energy imparted to the electron can range from nearly zero to a significant fraction of the incident photon energy. The relationship between the energy of the scattered photon and the scattering angle for a given interaction can be derived by solving simultaneous equations for the conservation of both energy and momentum:

$$h\nu' = \frac{h\nu}{1 + \frac{h\nu}{m_0c^2}(1 - \cos\theta)} \tag{1.4}$$

where m_0c^2 is the rest-mass energy of the electron. The energy transferred is independent of the density, atomic number, or any other characteristic of the absorbing material. Compton scattering is strictly an interaction between a photon and an electron. Only a minimal amount of energy is transferred for small scattering angles (θ). Regardless of the scattering angle, the incident photon always retains some of the original energy, even in the extreme case of $\theta = \pi$. The probability of Compton scattering per atom of the absorber depends on the number of electrons available as scattering targets and therefore increases linearly with the atomic number (Z).

1.1.1.0.3 Pair production: Pair production becomes energetically feasible when the photon energy exceeds twice the rest-mass energy of an electron (1.02 MeV). The probability of pair production remains low at energies that are only a few hundred keV above this threshold. However, this interaction mechanism becomes predominant at energies in the multi-MeV range. During the photon interaction, which must occur within the Coulomb field of a nucleus, the photon is annihilated and replaced by an electron-positron pair. As the positron subsequently decelerates within the absorbing medium, it undergoes annihilation, typically resulting in the emission of two annihilation photons as secondary products. These annihilation photons usually travel some distance before undergoing further interactions. In Figure 1.1, the graph shows representation of the relative predominance of the three main processes of photon interaction with absorber atom: photoelectric effect τ, Compton effect σ, and pair production k in a $(h\nu, Z)$ diagram where $h\nu$ is photon energy and Z is the absorber atomic number. The two curves connect points where photoelectric and Compton cross sections are equal ($\sigma = \tau$) and where Compton and pair production ($\sigma = k$) are equal. The total absorption cross-section, which represents the likelihood of a photon being removed from the primary beam, is obtained by summing the individual cross-sections of the photoelectric effect, Compton scattering, and pair production under narrow beam geometry conditions. This can be expressed as:

$$\sigma_{\text{abs}} = \sigma_{\text{photoelectric}} + \sigma_{\text{Compton}} + \sigma_{\text{pair production}} \tag{1.5}$$

Each process dominates at different energies, contributing to the overall probability of photon-matter interaction.

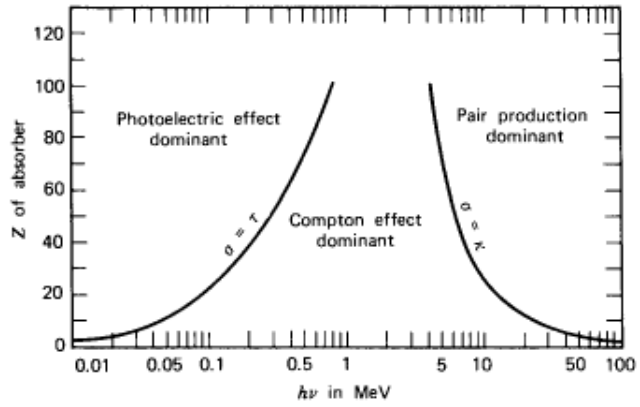

Figure 1.1: The relative significance of the three primary types of gamma-ray interactions. The lines represent the values of Z and hν where two adjacent interaction effects are equivalent [1].

1.1.1.0.4 Attenuation of photon beams: When monoenergetic photons pass through an absorber with varying thickness, the result is a simple exponential attenuation of the photon fluence. The interaction processes either absorb or scatter the photon out of the beam, and each method can be characterized by a specific probability of occurrence per unit path length in the absorber (see Eq.(1.5)). If we consider a photon beam with an initial intensity I_0 incident on a thick target, the intensity of the beam will decrease exponentially as it penetrates into the target, following the attenuation law:

$$I = I_0 \cdot e^{-\mu x} \qquad \text{with} \quad \mu = \rho \frac{N_A}{A} \sigma_{abs} \tag{1.6}$$

Where μ is the linear attenuation coefficient, x is the thickness of the medium, ρ is the density of the medium, N_A is the Avogadro number, A is the atomic mass number, and σ_{abs} is the total absorption cross-section. However, the use of the linear attenuation coefficient is constrained by its dependence on the absorber's density, even when the material remains the same. As a result, the mass attenuation coefficient is more commonly employed and is defined as

$$\text{mass attenuation coefficient} = \frac{\mu}{\rho} \tag{1.7}$$

The mass attenuation coefficient of a compound or mixture of elements can be determined by summing the mass attenuation coefficients of the individual elements, each weighted by their fractional mass contribution to the compound or mixture.

$$\left(\frac{\mu}{\rho}\right)_c = \sum_i w_i \left(\frac{\mu}{\rho}\right)_i \tag{1.8}$$

where w_i is the weight fraction of the i-th element in the compound or mixture.
In photon-based radiotherapy with kV X-ray beams, as illustrated in Figure 1.3, the absorbed dose in tissues decreases progressively with increasing depth. Kilovolt (kV) X-ray beams are suitable for treating superficial tumors and skin lesions due to their

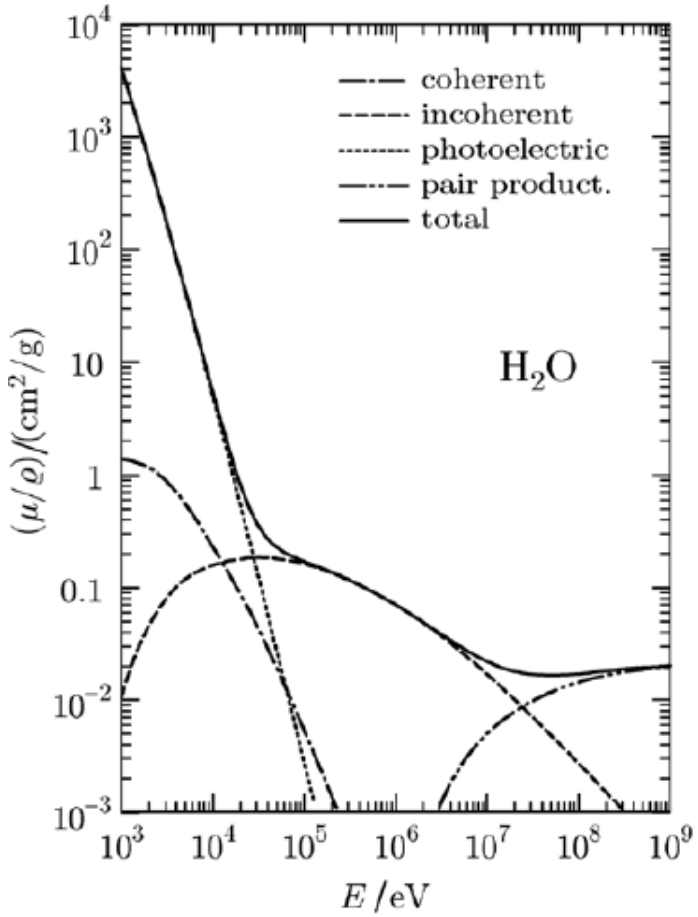

Figure 1.2: Partial and total mass attenuation coefficients for water plotted as functions of photon energy [2].

limited tissue penetration, which concentrates the dose near the surface, but they are not effective in treating deeper-seated tumors, because of their high surface dose and rapid dose falloff with depth. In contrast, megavolt (MV) beams provide greater tissue penetration, allowing the dose maximum to occur below the skin surface. The position of depth-dose maximum is directly related to the beam energy, meaning that higher-energy beams exhibit their maximum dose deposition at greater depths. This property makes MV beams more suitable for deep-seated tumors, delivering higher doses to the tumor while reducing exposure to superficial tissues, a phenomenon known as the skin-sparing effect.

1.1.2 Charged particles interaction mechanism

In contrast to photons, charged particles have electric charge and mass and dissipate their kinetic energy continuously through a series of successive interactions. These interactions give rise to phenomena such as ionization, excitation, molecular bond disruption, and nuclear fragmentation.

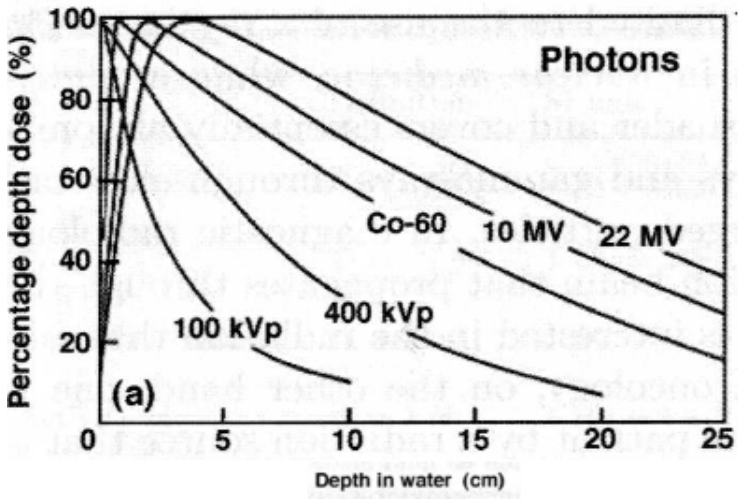

Figure 1.3: Percentage depth dose against depth in water for photon beams in the range from 100 kVp to 22 MV [3].

1.1.2.0.1 Stopping Power: The linear stopping power S, or specific energy loss, for charged particles in a given absorber is simply defined as the differential energy loss, for that particle within the material, per unit of path length:

$$S = -\frac{dE}{dx} \tag{1.9}$$

During particle traversal, energy deposition can be described by three primary mechanisms:

- Energy losses due to inelastic collisions with atomic electrons (collision stopping power, S_{col}).
- Energy losses due to energy transferred to the nuclei (nuclear stopping power, S_{nucl}).
- Energy losses due to the bremsstrahlung mechanism (radiative stopping power, S_{brem}).

For particles heavier than electrons, and with energies typically used in radiotherapy (below 500 MeV/n), most of the energy is lost through S_{col}. The nuclear stopping power, S_{nucl}, becomes relatively more important for ions with energies below 10 keV/n. S_{brem}, which is significant for electrons, is negligibly small for protons and heavier ions.
The mean specific energy loss by moderately relativistic charged heavy particles is well-described by the Bethe formula, which is written as follows:

$$\left\langle -\frac{dE}{dx} \right\rangle = Kz^2 \frac{Z}{A\beta^2} \left[\frac{1}{2} \ln \frac{2m_e c^2 \beta^2 \gamma^2 E_{\max}}{I^2} - \beta^2 - \frac{\delta(\beta\gamma)}{2} \right] \tag{1.10}$$

Where the coefficient for the expression is $K = 4\pi N_A {r_e}^2 m_e c^2$, N_A is the Avogadro's number, r_e is the classical electron radius and m_e the electron mass.The charge number of

incident particle is z, Z is the atomic number of absorber, A is the atomic mass of absorber and $\delta(\beta\gamma)$ represents density effect correction to ionization energy loss. The kinematic variables β and γ have their usual relativistic meanings; $\beta = \frac{v}{c}$ is the particle velocity relative to the speed of light and $\gamma = \frac{1}{\sqrt{1-\beta^2}}$ is the Lorentz factor. The parameter I corresponds to the mean excitation and ionization potential of the absorber, typically treated as an experimentally determined constant for each element. $E_{\max}$ is the maximum energy transfer in a single collision for a particle with mass M,

$$E_{\max} = \frac{2m_e c^2 \beta^2 \gamma^2}{1 + 2\gamma m_e/M + (m_e/M)^2} \tag{1.11}$$

Equation (1.10) is valid in the region $0.1 \lesssim \beta\gamma \lesssim 1000$ with an accuracy of a few percent. The stopping power of a particle is directly proportional to the square of its charge therefore a particle with a higher atomic number, such as the C^{12} ion, releases more energy for the same thickness. At low energy, S is approximately proportional to β^{-2}; therefore, the greatest energy loss occurs when the particle is nearly at rest. This behavior leads to the characteristic Bragg peak observed in the depth-dose distribution, where the energy deposition reaches its maximum just before the particle comes to a stop.

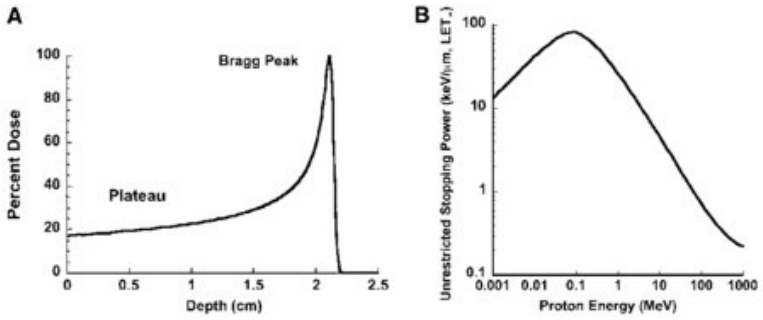

Figure 1.4: Percentage depth dose distribution for 50-MeV protons, illustrating: (a) the characteristic plateau and Bragg peak regions; (b) the unrestricted collisional stopping power of incident protons as a function of their energy [4].

1.1.2.0.2 Particle range: Charged particles are characterized by a definite range in a given absorber material. The particle range is defined as the actual depth traveled by the particle within the target medium. Assuming the slowing down of the particle as a continuous process, the continuous slowing down approximation (CSDA) can be used to determine the mean range of the particle based only on their stopping power and their initial energy E_0.

$$R_{\text{CSDA}}(E) = \int_0^{E_0} \left(\frac{dE}{dx}\right)^{-1} dE \tag{1.12}$$

Comparison of the ranges of various ions of therapeutic interest are shown in Fig.1.5 which emphasizes how the mean range of different particles with the same specific energy scales

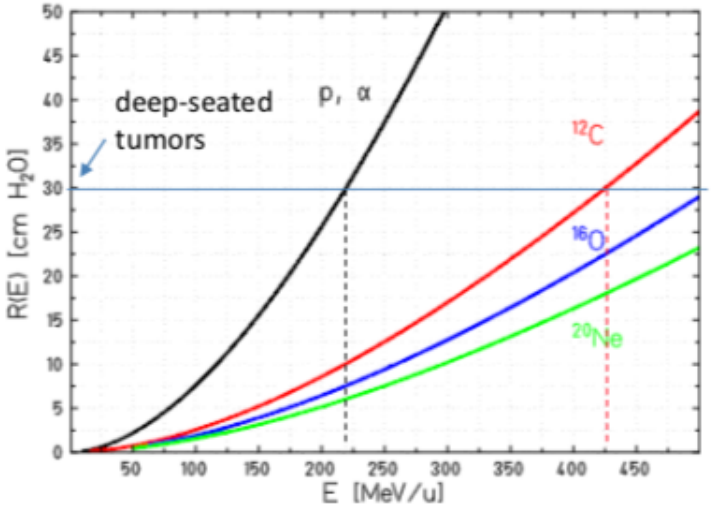

Figure 1.5: Mean range of heavy ions in water [5].

with a factor of $\frac{A}{Z^2}$. Charged particles experience energy straggling, which refers to the statistical fluctuations in the energy deposition by individual ions. Statistical fluctuations in the energy loss during the numerous collisions in the slowing-down process result in the broadening of the Bragg peak for an ion beam composed of multiple particles. The same stochastic factors that cause energy straggling at a given penetration depth also result in slight variations in the total path length of each particle. For heavy charged particles, such as protons or carbon ions, the extent of this straggling is typically a few percent of the mean range. The shape of the relative energy loss probability density function $f(\Delta E)$ depends on the following parameter:

$$k = \frac{\overline{\Delta E}}{E_{\max}}. \tag{1.13}$$

Where $\overline{\Delta E}$ is the mean energy loss and $E_{\max}$ the maximum energy loss possible in a single event. For thick targets ($k \geq 10$), the projectile undergoes numerous interactions, losing only a small fraction of its energy in each collision with the target's electrons. In such cases, the energy loss distribution can be effectively approximated by a Gaussian distribution.

$$f(\Delta E) = \frac{1}{\sqrt{2\pi\sigma_E}} \exp\left(-\frac{(\Delta E - \overline{\Delta E})^2}{2\sigma_E^2}\right) \tag{1.14}$$

with

$$\sigma_E = 4Z_{\text{eff}} Z_t e^4 N \Delta x \left(\frac{1 - \beta^2/2}{1 - \beta^2}\right) \tag{1.15}$$

For thinner targets ($0.01 \leq k \leq 10$), the Vavilov distribution is typically applied, while for very thin targets ($k \leq 0.01$), the Landau distribution is used. The variance σ_R^2 of range

straggling is related to the variance σ_E^2 of energy-loss straggling by the equation:

$$\sigma_R^2 = \int_0^{E_i} \left(\frac{d\sigma_E}{dx}\right) \left(\frac{dE}{dx}\right)^{-3} dE \tag{1.16}$$

The ratio of the straggling width σ_R and the mean range R is nearly constant and can be described by:

$$\frac{\sigma_R}{R} = \frac{1}{\sqrt{M}} f\left(\frac{E}{Mc^2}\right) \tag{1.17}$$

Where f is a slowly varying function depending on the absorber, and E and M are the particle energy and mass. Due to the $\frac{1}{\sqrt{M}}$ dependence the relative straggling is smaller

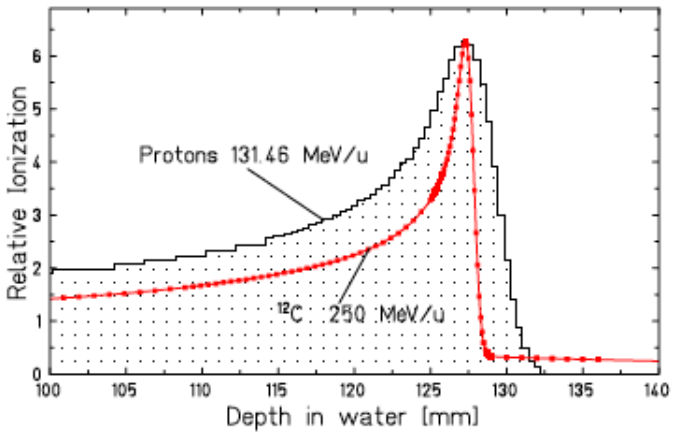

Figure 1.6: Bragg peaks measured for protons and C^{12} ions with identical mean ranges in water [5].

for heavier ions than for protons, as shown in Fig.1.6.

1.1.2.0.3 Lateral scattering: Charged particles, in addition to undergoing inelastic collisions, also experience elastic Coulomb collisions, which cause deflections in the particle's trajectory. For hadrons, small-angle scattering is significantly more probable than large-angle deflections, and the cumulative effect of numerous collisions results in a lateral spread of the beam and angular divergence. This phenomenon is referred to as Multiple Coulomb Scattering (MCS). The fundamental scattering mechanism is described by the Rutherford cross section, which is expressed as a function of angle Θ.

$$\frac{d\sigma}{d\Omega} \propto \frac{Z_p^2 Z_t^2}{E^2 \sin^4\left(\frac{\Theta}{2}\right)} \tag{1.18}$$

This equation illustrates that the scattering cross section increases with the projectile's charge, but decreases significantly with higher energy. Furthermore, Eq.(1.18) shows that the cross section decreases rapidly as the scattering angle increases, indicating that during the traversal of a medium, a charged particle undergoes numerous scattering events,

predominantly with very small scattering angles. The cumulative effect of these multiple scattering events causes the particle beam to broaden as it passes through the medium, a phenomenon described by Molière's theory of scattering [17], which provides an analytical solution to Eq.(1.18). The resulting probability distribution of the scattering angles is often approximated by a Gaussian function, which provides an accurate representation for small angles but underestimates the probabilities associated with the less frequent 'hard' scattering events, which correspond to larger deflection angles:

$$F(\Theta, \sigma) = 2\pi \frac{\Theta}{\sigma^2} \exp\left(-\frac{\Theta^2}{2\sigma^2}\right) d\Theta \tag{1.19}$$

with the standard deviation σ that can be calculated using a Gaussian approximation for the central 98% of the projected angular distribution, using the following formula given by Lynch & Dahl ([19]).

$$\sigma_\theta = \frac{13.6\,\text{MeV}}{\beta c p} z \sqrt{\frac{x}{X_0}} \left[1 + 0.088 \log_{10}\left(\frac{x^2}{X_0 \beta^2}\right)\right] \tag{1.20}$$

Where p, βc, and z are the momentum, velocity, and charge number of the incident particle, and $\frac{x}{X_0}$ is the thickness of the scattering medium in radiation lengths. Equation (1.20) provides an accurate description for small values of Z; however, for large values of Z and small values of x, its representation becomes less accurate. Typically, the problem

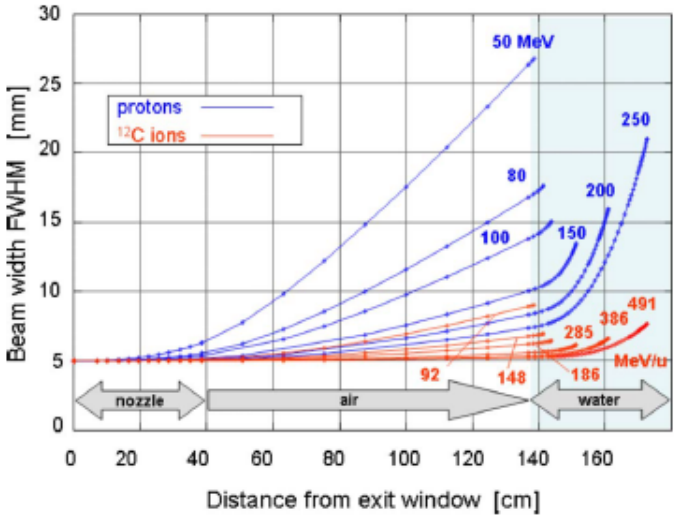

Figure 1.7: Calculated beam spread for C^{12} ions and protons in a typical treatment beam line. Carbon ions exhibit a significantly smaller spread compared to protons at the same penetration depth [5].

involves the multiple scattering of a particle traversing several distinct layers, whereas Eq.(1.20) describes scattering in a single material. To account for this difference, it is significantly more accurate to apply Eq.(1.20) only once, after determining the combined values of x and X_0 for the composite scatterer. Targets composed of heavier elements

induce a greater angular spread compared to those made of lighter elements, even when the thickness is identical. While the angular spread for heavy charged particles remains relatively small, it increases significantly at lower energies due to the factor $\frac{1}{\beta cp}$ in the Eq.(1.20). In clinical practice, the two main contributions to angular beam spreading that must be considered are: scattering caused by materials placed in front of the patient, such as range shifters and immobilization masks, and scattering within the tissue between the entry point and the stopping depth. Therefore, for low-energy particles, the material in the beam path in front of the patient should be kept as thin as possible, not contain heavy elements, and should be placed as close to the patient as possible. However, for high-energy particles, inhomogeneities in the tissue can cause significant broadening of the beam. Figure 1.7 illustrates the behavior of a charged particle beam in a typical radiotherapy configuration. In this simulation, a parallel beam of ^{12}C ions or protons passes through the nozzle and subsequently enters the body of the patient, represented here by a water absorber. At shallow depths, the beam width is mainly influenced by scattering within the nozzle. However, at higher energies, the scattering within the water absorber becomes the dominant factor.

1.1.2.0.4 Nuclear fragmentation: Protons and ions within the clinical energy range have a significant likelihood of undergoing non-elastic nuclear interactions. Nuclear collisions do not affect the position of the Bragg peak, although they are responsible for the loss of fluence of the primary particles, fragment production, and emerging secondary particles, which decrease, broaden, and create a tail in the Bragg curve. The key distinction between proton and ion beams lies in the type of fragmentation: for protons, only target fragmentation occurs, whereas for heavier ions, projectile fragmentation is the dominant process. In proton-induced reactions, unstable nuclei are generated following absorption,

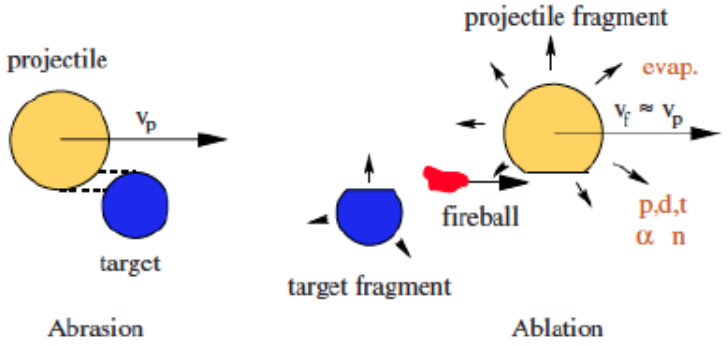

Figure 1.8: Illustration of the abrasion-ablation model for peripheral collisions at high energies.[5]

which subsequently emit one or more secondary protons. Additionally, secondary neutrons and gamma rays are released during de-excitation processes, along with a smaller quantity of heavier recoil nuclei. The dose associated with these recoils is generally assumed to be absorbed at the site of production. Secondary protons are predominantly generated at wider angles, which contributes to a halo of secondary protons around the

primary beam. The production of secondary neutrons poses a particular concern due to their high relative biological effectiveness (RBE), especially in delayed effects within healthy tissue, such as the induction of secondary cancers. The cross sections for proton interactions are greatest at high energies, leading to an increased production of secondary particles at these energy levels. An additional point of significance is that the more material present in the primary beam, the more secondary particles are generated. For ions,

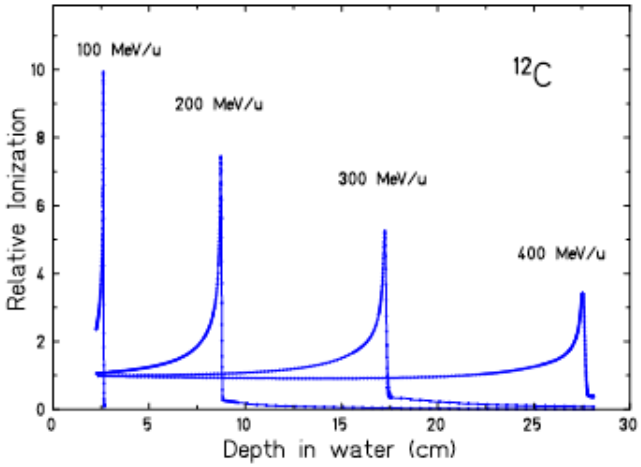

Figure 1.9: Measured Bragg curves of ^{12}C ions stopping in water [5].

projectile fragments have a greater range because they are produced at the same velocity as the primary ions but possess a lower mass, resulting in a fragmentation tail beyond the Bragg peak. In the case of carbon ions, inelastic nuclear interactions not only lead to attenuation of the primary particle number and fragment formation but also create a halo of lighter fragments emitted at an angle relative to the trajectory of the primary ions. Due to their lower charge, however, the dose deposited by this halo is relatively small. The impact of nuclear fragmentation on the dose-depth profile is depicted in Fig. 1.9. As the penetration depth increases, the ratio of the peak dose to the entrance dose diminishes progressively, primarily due to the exponential decrease in the flux of ^{12}C ions. The accumulation of lower atomic number (Z) fragments is distinctly visible in the dose tail beyond the Bragg peak at greater depths. Additionally, the broadening of the Bragg peaks is more pronounced due to the energy straggling effect, leading to a wider distribution of dose deposition.

A key challenge is the limited availability of experimental data on ion beam fragmentation in human tissues. As a result, Monte Carlo simulations are frequently employed to model these effects, contributing to treatment planning and ensuring safety in therapy. Moreover, as previously discussed, the primary advantage of using charged particles in radiotherapy lies in their unique depth-dose distribution, characterized by the Bragg peak. This depth-dose profile is marked by a low initial dose upon entry, a distinct dose maximum (the Bragg peak) close to the end of the particle's range, and a rapid dose decline at the distal edge (see Fig. 1.10). By concentrating the radiation dose precisely at the tumor site, the energy deposition can be controlled to reach its peak within the cancerous tissue, minimizing exposure to adjacent structures. Unlike photon beams, charged particles do

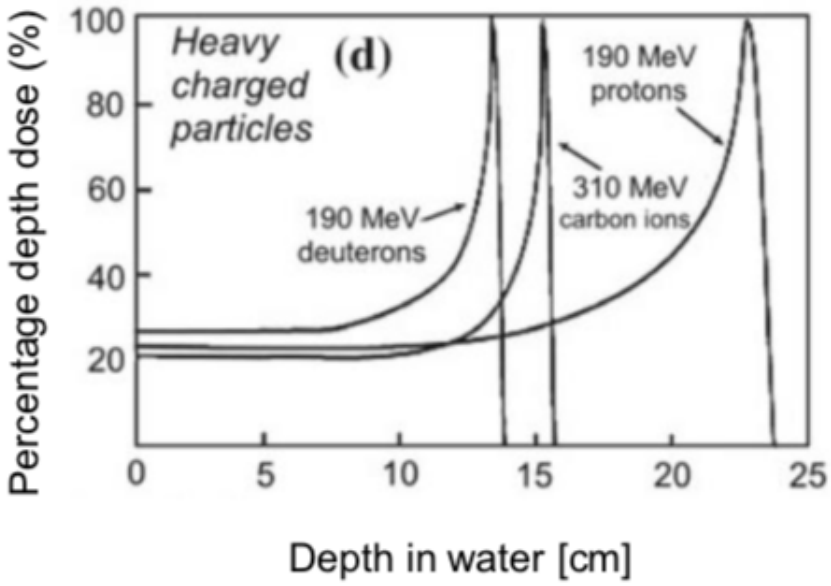

Figure 1.10: Depth-dose curves in water for heavy charged particles [3].

not produce a dose tail from bremsstrahlung radiation due to their significantly larger mass relative to electrons. However, in the case of carbon ions, nuclear interactions can generate secondary particles, which contribute to an extended dose tail beyond the Bragg peak.

1.1.2.0.5 Spread out Bragg peak: The unmodified Bragg peak generated by a monoenergetic ion beam is too narrow to cover a tumor effectively in clinical applications. To achieve homogeneous dose distribution across the entire target volume, a technique known as the Spread Out Bragg Peak (SOBP) is used. This approach superimposes multiple Bragg peaks of varying ranges by adjusting the entrance energies and intensities of the ion beams during irradiation. The SOBP allows for precise dose distribution at depth, maintaining uniform coverage throughout the target volume. However, a drawback is that the overlapping of dose curves also occurs in the proximal region of the tumor, leading to an increase in dose to adjacent healthy tissue. Despite this effect, the SOBP technique still provides a significant dose-saving advantage in the proximal region compared to photon irradiation. As illustrated in figure 1.11, achieving the same planned dose to the target volume requires a far higher proximal dose with photons than with protons. The SOBP method does not disadvantage the distal region either, as the dose profile maintains a steep fall-off at the edge of the target volume, thereby minimizing radiation exposure to healthy tissue beyond the tumor.

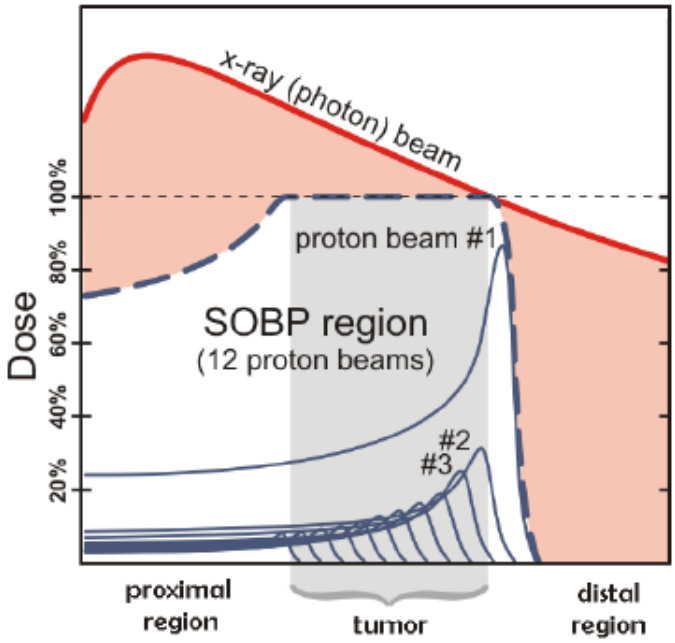

Figure 1.11: Depth–dose distributions for a spread-out Bragg peak (dashed blue), its constituent pristine Bragg peaks (solid blue), and a photon beam (red) [6].

1.2 Water-equivalent path length (WEPL) and Hounsfield units (HU)

In order to facilitate a thorough understanding of the subsequent discussion, it is necessary to introduce a series of dosimetric and radiobiological quantities. These parameters are critical for establishing the connection between the physics governing particle interactions and their clinical application in particle therapy. To accurately calculate dose deposition, including the precise location of the Bragg peak in heterogeneous tissues, it is essential to establish the relationship between CT numbers, ion stopping power, and water-equivalent path length (WEPL). The WEPL represents the equivalent distance that a particle beam would need to travel in water to experience the same energy loss as it does when passing through a given tissue. As illustrated in Fig.1.12, the grayscale levels in digital CT images are represented by CT numbers, also known as Hounsfield units (HU), which quantify the attenuation of X-rays relative to water. HU values are defined as:

$$\mathrm{HU} = \left(\frac{\mu_{\mathrm{material}} - \mu_{\mathrm{water}}}{\mu_{\mathrm{water}} - \mu_{\mathrm{air}}} \right) \times 1000; \tag{1.21}$$

where μ_{material} and μ_{water} are the linear attenuation coefficients of the material and water, respectively, and μ_{air} is the linear attenuation coefficient of air, which is approximately zero and can therefore be neglected. The Hounsfield scale allows for the representation of the local density of tissues in relation to water, which is taken as a reference due to its fundamental role in human biological composition. By definition, air has a CT number

of -1000 HU, while water has 0 HU, and all other tissues are scaled accordingly. Since

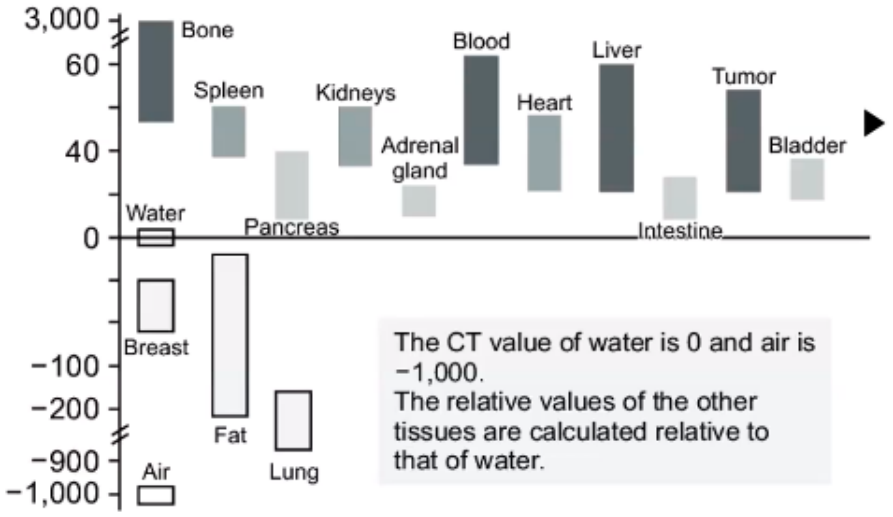

Figure 1.12: Hounsfield scale of computed tomography (CT) numbers for various tissues [7].

theoretical HU values and experimentally obtained HU values from CT scans are not always identical, a calibration process is necessary to accurately convert HU into WEPL. This calibration ensures that the WEPL values reflect the actual energy loss experienced by the particle beam in different tissues. The process involves calibration phantoms (see Fig.1.13, top), which contain materials with known densities that mimic different tissue types (e.g., lung, muscle, fat, and bone). These phantoms allow for the experimental measurement of the residual energy loss of a proton beam passing through each material, thereby determining the corresponding WEPL values. The calibration curve (Fig.1.13), derived from these phantom measurements, converts the voxel density from HU to WEPL coefficients. This method standardizes the measurement of the depth reached by particles in heterogeneous tissues. Since tissue densities vary, the geometric path of the particle in a medium with density different from water is converted into an equivalent path in water by multiplying the actual path length by a scaling coefficient. This coefficient is defined as the ratio of the tissue density to the density of water:

$$l_{\text{WEPL}} = \frac{\rho_{\text{tissue}}}{\rho_{\text{water}}} \cdot l_{\text{actual}} \tag{1.22}$$

During the calibration process, approximately ten reference points are measured to represent the conversion from HU to WEPL for different densities, with intermediate values obtained through linear interpolation. This ensures that voxel densities are accurately expressed in terms of WEPL, allowing for precise localization of the Bragg peak and dose delivery calculations. If the HU-to-WEPL conversion were inaccurate, it could lead to a misalignment of the Bragg peak, potentially resulting in suboptimal dose delivery to the tumor or unintended exposure of healthy tissues. Therefore, the calibration process is a critical step in particle therapy planning.

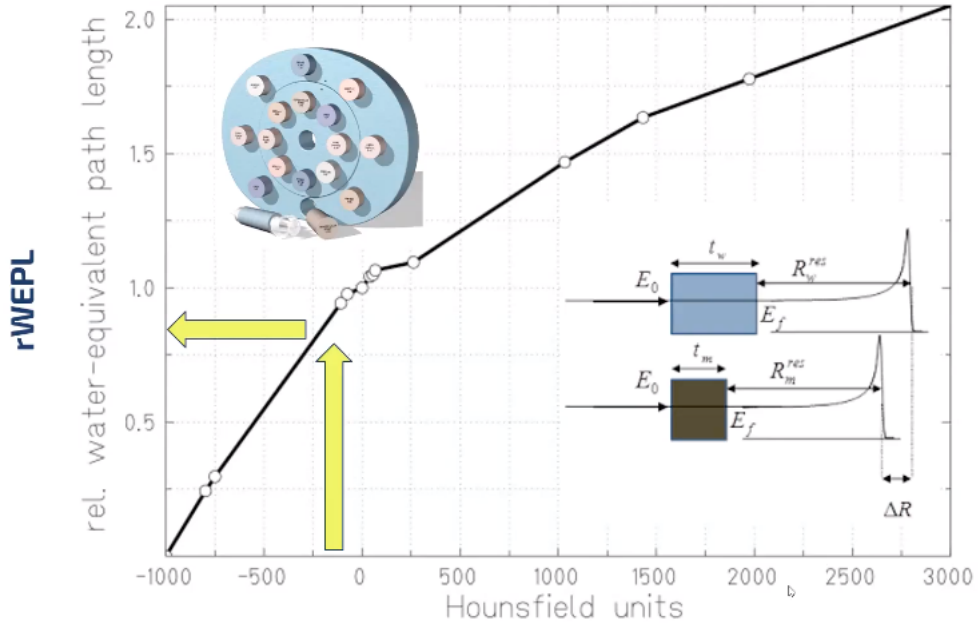

Figure 1.13: Calibration curve obtained from CT scans of a phantom to convert Hounsfield units (HU) into water-equivalent path length (WEPL). Top: The calibration phantom consists of materials with known densities designed to simulate different human tissues (e.g., lung, muscle, fat, bone). Each material's HU value is measured and paired with its corresponding experimentally determined WEPL. Bottom: Comparison between the energy loss of a particle beam passing through different materials and an equivalent thickness of water, highlighting the corresponding shift in the Bragg peak due to differences in stopping power [8].

1.3 Linear energy transfer

Absorbed dose is a fundamental quantity in radiotherapy; however, it is not sufficient to determine the biological effects of radiation, as these also depend on the type of radiation and its spatial distribution within the tissue. To account for these factors, Linear Energy Transfer (LET) is employed to specify the quality of ionizing radiation. The LET is defined as the mean amount of energy that a given ionizing radiation imparts to an absorbing medium per unit of path length. It describes how densely the radiation deposits its energy along its track.

$$LET_{\Delta} = \frac{dE_{\Delta}}{dl} \qquad \text{Unit: } keV \cdot \mu m^{-1} \tag{1.23}$$

Where dE_{Δ} is the average energy lost in dl through excitation and ionization processes in which the energy transferred to the liberated electrons (the secondary electrons) does not exceed a predetermined Δ limit. As Δ approaches infinity, the LET becomes nominally identical to the electronic stopping power and is denoted by the symbol: LET_{∞}. In contrast to the electronic part of the stopping power, which focuses attention on the energy loss by an energetic charged particle moving through an absorber, the LET focuses on the energy absorption by the absorbing medium as the charged particle traverses the absorber. Based on the ionization density produced within the absorber, ionizing radiation can be classified into two distinct types: low LET radiation (sparsely ionizing) with LET $< 10 keV \cdot \mu m^{-1}$ and high LET radiation (densely ionizing).

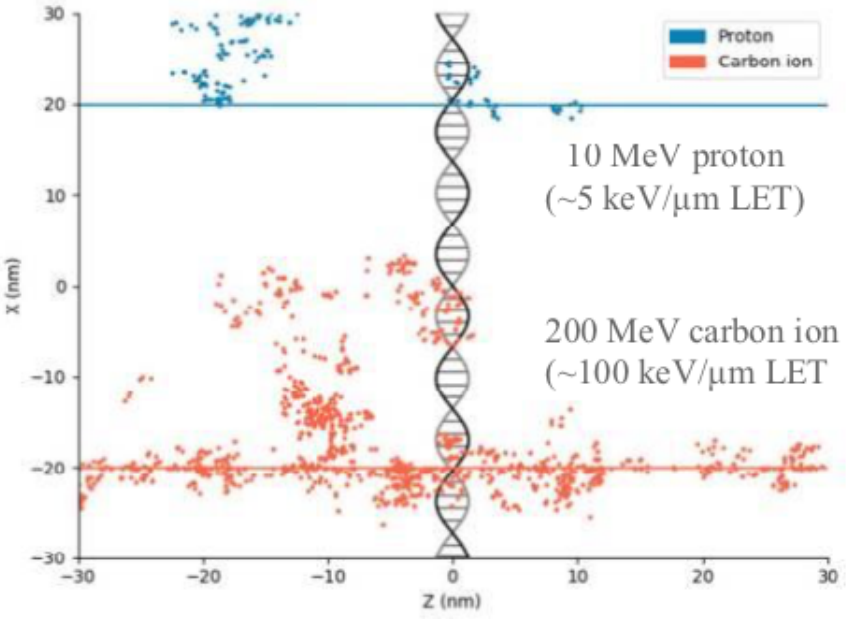

Figure 1.14: Illustration of the track structure and energy deposition distributions for a proton and a carbon ion, along with a schematic representation of DNA as a scale reference [9].

In order to understand the clinical significance of high versus low LET radiation, it

is crucial to recognize that, when ionizing radiation interacts with biological tissue, both primary physical interactions and secondary chemical-biological effects must be considered. Radiation-induced damage is triggered by physical interactions occurring within 10^{-18} to 10^{-12} seconds post-irradiation, initiating a cascade of processes that may result in the formation of free radicals or the activation of complex enzymatic mechanisms. These processes can result in changes to the chemical composition of molecules and biofunctional modifications, such as mutations and cell death. DNA is the primary target for the biological effects of radiation, which include cell death, carcinogenesis, and mutation [21]. Structurally, DNA is a large molecule organized into a double helical structure consisting of two strands, separated by a distance of approximately 2-3 nm, made up of alternating sugar (deoxyribose) and phosphate groups. Attached to these, are four bases (adenine, thymine, guanine, and cytosine) whose sequence encodes genetic information. DNA replication is central to cellular division, making it a crucial target in cancer therapy. In the case of cancerous cells, therapeutic interventions aim to damage the DNA of these cells, ultimately leading to cell death and the cessation of uncontrolled proliferation. Ionizing radiation can induce various forms of DNA damage, including base damage (base loss and base modification), single-strand breaks (SSBs), double-strand breaks (DSBs), and DNA-protein crosslinks. Although cells possess several pathways to repair DSBs, these pathways are generally more error-prone compared to those that repair simpler lesions, such as base damage or SSBs. Radiation-induced cell death is strongly correlated with the number of double-strand breaks (DSBs), particularly complex DSBs, which occur when additional damage is present near the primary break. For low-LET radiation, approximately 30% of DSBs are classified as complex. Conversely, with high-LET radiation, this percentage increases significantly to 70%, as the higher energy density deposited along the radiation track leads to more localized and complex DNA damage [22]. Since DNA

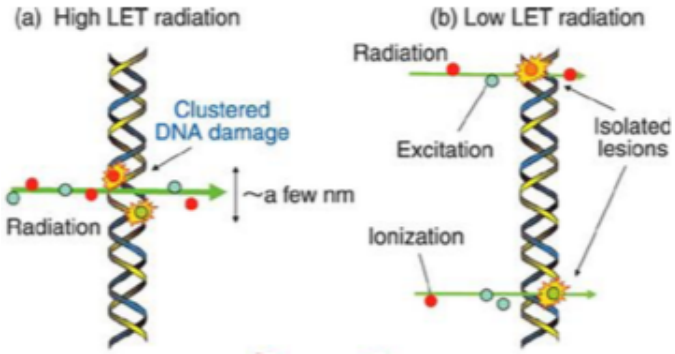

Figure 1.15: Induction of DNA damage by ionizing radiation [10].

occupies a small portion of the cell volume, while approximately 80% consists of water, most of the energy absorbed by cellular tissue leads to ionization and excitation of H_2O molecules. This process results in the formation of free radicals, which mediate indirect DNA damage by diffusing far enough to reach and attack critical cellular targets. For high-LET radiation the energy is deposited in a highly concentrated manner along the particle's track, directly initiating the breaking of chemical bonds. In general, protons, and more notably carbon ions, produce a greater number of direct interactions compared

to photons, which, due to their lower LET, are more likely to interact indirectly with DNA.

1.4 Linear quadratic model

Experimental measurements of cell survival are conducted to assess the effectiveness of a particular type of radiation in inducing cell death. Cells cultured in vitro are irradiated with different types of radiation to estimate the surviving fraction (see Fig. 1.16), which is defined as follows:

$$\text{Surviving fraction} = \frac{\text{Colonies counted}}{\text{Cells seeded} \times (PE/100)} \tag{1.24}$$

Where Plating Efficiency (PE) evaluates how many of the seeded cells naturally form colonies, providing a baseline for comparison.

$$PE = \frac{\text{Number of colonies counted}}{\text{Number of cells seeded}} \times 100 \tag{1.25}$$

Typically, cell survival is represented graphically by plotting the logarithm of the survival

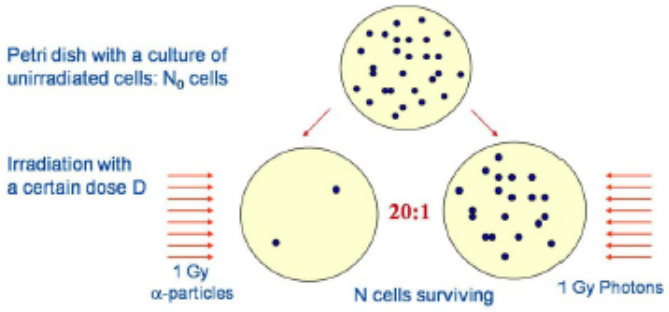

Figure 1.16: Survival fraction of cell cultures following exposure to two different types of radiation.

fraction (S) as a function of the absorbed dose. The most widely used model for describing the relationship between dose and cell survival is the linear-quadratic (LQ) model.

$$S = e^{-(\alpha D + \beta D^2)} \tag{1.26}$$

This model is expressed in terms of the dose,D, and two parameters: α and β describing the cell's radiosensitivity. As illustrated in Figure 1.17 the survival fraction plotted on a log scale, gives a quadratic response curve. This is commonly referred to as a "shouldered" dose-response curve, where the initial response is predominantly linear at lower doses, characterized by the α term. As the dose increases, the quadratic contribution represented by the βD^2 term becomes more prominent, leading to increased curvature in the dose-response relationship. The extent of this curvature is typically defined by the α/β ratio, expressed in units of Gray (Gy). This ratio corresponds to the dose level at which the

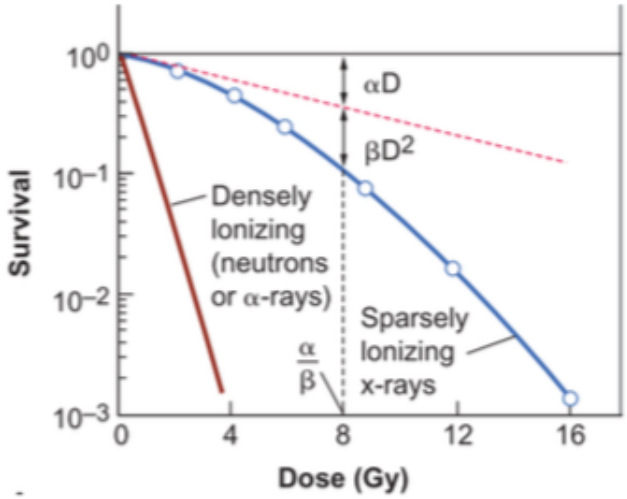

Figure 1.17: Shape of survival curve for mammalian cells exposed to radiation. The experimental data are fitted to a linear-quadratic function. The fraction of cells surviving is plotted on a logarithmic scale against dose on a linear scale [11].

linear and quadratic components contribute equally to cell damage. Cells with a high α/β ratio exhibit a relatively constant rate of cell death as the radiation dose increases, indicating a predominant contribution from the linear component. In contrast, cells with a low α/β ratio display a more pronounced curvature in their dose-response curve, reflecting a higher sensitivity at increased doses. The α term in the model represents cell death caused by 'single-hit' events, where a single radiation particle delivers sufficient energy to induce lethal damage in the cell. This is typical in high-LET radiation scenarios. On the other hand, the β term accounts for 'multiple-hit' cell death, where the interaction of damage from different radiation tracks accumulates, with the effect scaling quadratically with the dose.

1.4.1 Fractionation in radiotherapy

The linear-quadratic model not only accurately reflects cellular survival in vitro but also offers a consistent interpretation of clinical fractionation effects in tissues and tumors, where the total radiation dose is divided into multiple fractions. In fractionation, cells have the opportunity to repair sub-lethal damage between fractions. This phenomenon is captured by the curvature of the LQ model, quantified by the α/β ratio, measured in Gray. The α/β value helps differentiate tissue sensitivity to fractionation: tissues with a low α/β ratio benefit more from fractionation in terms of sparing compared to those with a higher ratio, as illustrated in Fig.1.18. In the case of X-rays or γ-rays (characterized by a low α/β ratio), fractionating the radiation into smaller doses over time intervals allows more cells to survive due to the time-dependent repair of sub-lethal damage. Summarizing, the linear α-component represents lethal damage from single-event hits that are independent of time and unaffected by fractionation or dose rate. In contrast, the quadratic β component accounts for cell death due to cumulative damage, which can be

mitigated through fractionation or by reducing the dose rate, thus allowing cells to repair before accumulating irreversible damage. Based on their response to radiation, affected

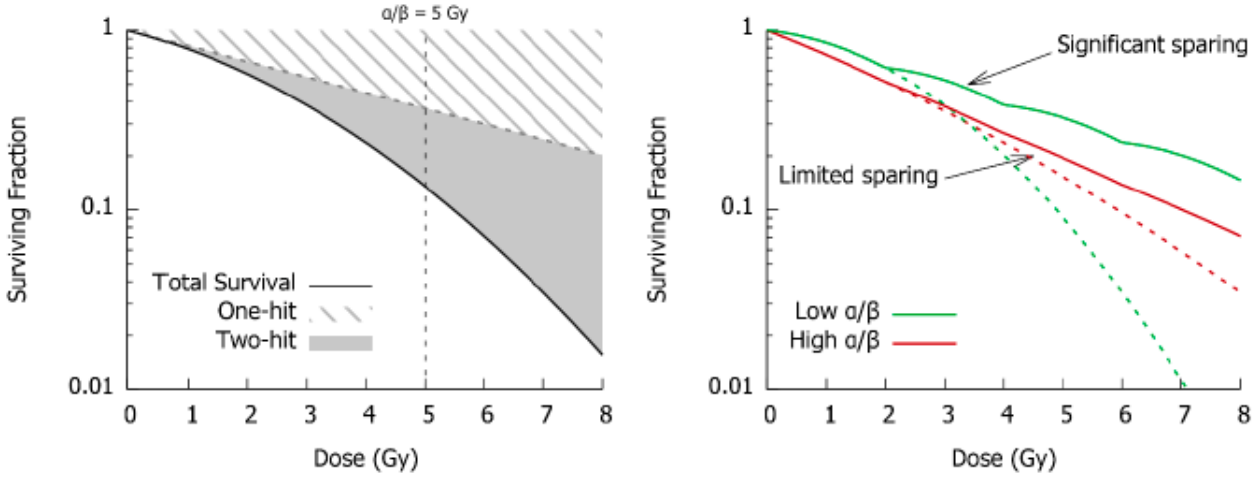

Figure 1.18: Left: illustration of the linear-quadratic dose-response model, which postulates that cell survival consists of a linear "one-hit" component and a quadratic "two-hit" component. These components contribute differently depending on the radiation dose. Right: the illustration provides an intuitive explanation of the benefits of fractionation. In tissues with a low α/β ratio, the "shoulder" of the curve is repeated with each fraction, leading to significant tissue sparing. In contrast, tissues with a high α/β ratio exhibit much less sparing [9].

tissues are classified as either early, responding or late-responding. Organs with rapidly proliferating cells, such as the skin, oral mucosa, and bone marrow, tend to exhibit low sensitivity to fraction size and show symptoms during or immediately following radiotherapy. These early-responding tissues are characterized by high α/β ratios, typically around 7–10 Gy. In contrast, organs with slower cellular turnover, such as the heart, lungs, and kidneys, respond over extended periods, ranging from months to years, and demonstrate increased sensitivity to fraction size. Late-responding tissues typically have α/β ratios within the range of 3–5 Gy. Cancerous tissues, characterized by uncontrolled cellular proliferation, are expected to have a high α/β ratio, estimated around 10 Gy, similar to that of early-responding tissues. Consequently, fractionation allows for sparing of slowly dividing normal tissues, enabling an escalation of the tumor dose without causing unacceptable toxicity in surrounding normal tissues.
The LQ model provides insights into the varying impact of fractionation and the specific responses of different treated tissues. This approach highlights that the observed effect, or clinical effect level, depends solely on the fraction of surviving cells. This assumption proves highly useful in clinical practice, as it enables comparison of the clinical effects of treatments performed with different fractionation schedules. Given a level of effect E in response to a treatment with n fractions of dose d, where $D = nd$ represents the total dose delivered, we obtain:

$$E = -\ln(S) = n(\alpha d + \beta d^2) = D(\alpha + \beta d) \tag{1.27}$$

This highlights the sparing effect of fractionation: by keeping the total dose D constant but increasing the number of fractions n (thus reducing the dose per fraction d), the biological effect on healthy tissues also decreases accordingly. The degree of sparing is dependent on the α/β ratio of the target population, as shown in the following equation:

$$E = \alpha D \left(1 + \frac{d}{\alpha/\beta}\right) \tag{1.28}$$

The magnitude of the effect can therefore be represented as the product of a term inde-

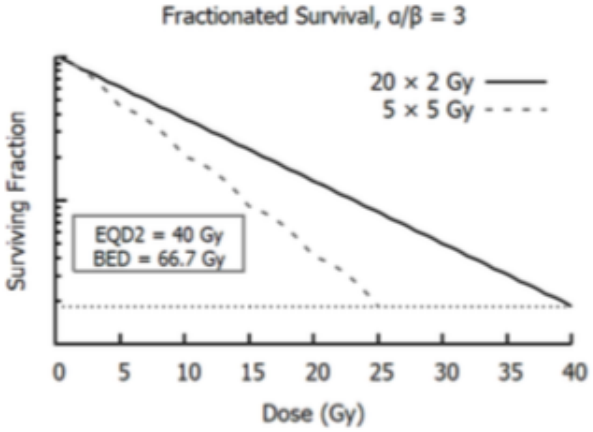

Figure 1.19: Illustration of iso-effective LQ treatment schedules for a tissue with $\alpha/\beta = 3$. A regime of 20 fractions at 2 Gy each achieves the same level of cell killing as 5 fractions at 5 Gy each. These schedules are iso-effective, having identical equivalent doses in 2 Gy fractions (EQD2) and biologically effective doses (BED), as shown in the inset [12].

pendent of fraction size, associated with the total dose (αD), and a term dependent on fraction size, which inversely scales with the α/β ratio. Two commonly used concepts for comparing different radiotherapy fractionation regimes are introduced here: the Equivalent Dose in 2 Gy Fractions (EQD2) and the Biologically Effective Dose (BED). Given the widespread use of 2 Gy fractionation schedules, treatments are frequently compared based on the equivalent dose in 2 Gy fractions (see Fig. 1.19). To calculate the EQD2 for an arbitrary schedule of n fractions with dose d, the dose required to produce an equivalent level of effect is determined.

$$\alpha D \left(1 + \frac{d}{\alpha/\beta}\right) = \alpha\,\mathrm{EQD2} \left(1 + \frac{2}{\alpha/\beta}\right) \tag{1.29}$$

From which it follows:

$$\mathrm{EQD2} = D \left(\frac{d + \alpha/\beta}{2 + \alpha/\beta}\right) \tag{1.30}$$

The BED is a metric used to compare the biological efficacy of radiotherapy treatments with varying fractionation schemes, without being restricted to a specific dose per fraction. While EQD2 relies on 2 Gy fractions, BED assumes an infinitesimally small fraction size,

making it a useful parameter for comparing treatments based on "pure" biological damage, unaffected by fractionation effects. In the limit where fraction size approaches zero, the contribution of “multi-hit” events becomes negligible, and BED is calculated by dividing the effect level E by the α term:

$$\text{BED} = \frac{E}{\alpha} = D\left(1 + \frac{d}{\alpha/\beta}\right) \tag{1.31}$$

1.5 Relative biological effectiveness

The biological effectiveness of photon radiation is well-documented due to extensive studies and experimental data. However, there is comparatively less direct experience with high-LET radiation. To address this gap and enable meaningful comparisons between photon and high-LET radiation, the concept of Relative Biological Effectiveness (RBE) is introduced. RBE quantifies the biological efficacy of high-LET radiation in relation to photon radiation, allowing for the evaluation of dose-response relationships across different types of radiation.

$$RBE_r = \frac{D_{250\text{ kV x-rays}}}{D_r} \tag{1.32}$$

where $D_{250\text{ kV x-rays}}$ is the dose of 250 kV x-rays required to produce a certain biological effect [13], and D_r is the dose of the radiation being compared to achieve the same biological effect. For photons, the initial decline in cell survival as a function of dose is more

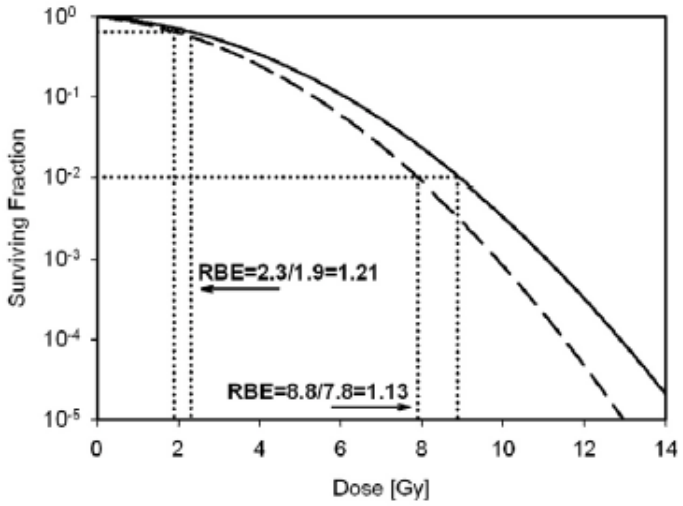

Figure 1.20: Dose-response curves for photon radiation (solid line) and proton radiation (dashed line), illustrating the RBE at two effect levels [14].

gradual compared to ions. As a result, RBE tends to increase as cell survival rises and the dose decreases. The RBE is strongly influenced by both the dose and the LET. Initially, the RBE increases as LET increases, as the number of ionizing events rises, thereby enhancing biological effectiveness (see Fig.1.21). RBE reaches its peak at approximately

100 keV/µm, which corresponds to the LET at which the average distance between two ionizing events is on the order of nanometers, equivalent to the size of the DNA molecule, maximizing the likelihood of direct DNA damage. However, as LET continues to increase beyond this threshold, the additional ionization events no longer contribute to greater biological effectiveness. This results in what is known as the "overkill" effect, where the excess ionizations become redundant. Consequently, although the deposited dose continues to rise, the RBE decreases, as RBE is defined as the ratio between the dose of a reference radiation and that of high-LET radiation required to produce the same biological effect.

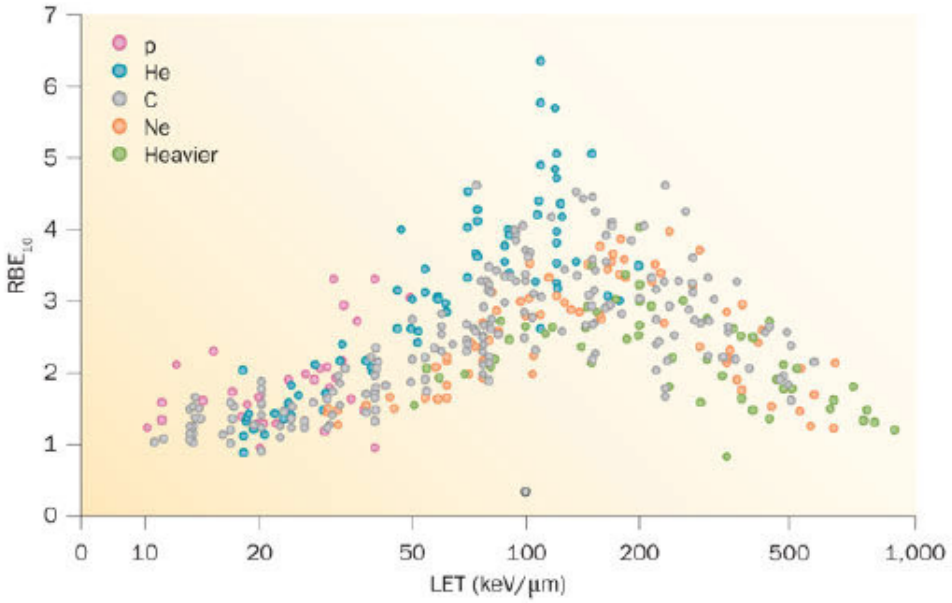

Figure 1.21: RBE as a function of LET from experiments on in vitro cell lines, as reported in [15].

1.5.1 Radiobiological Model: The Local Effect Model (LEM)

The RBE can vary significantly depending on several factors, including the type and energy of the particles, the delivered dose, and the LET. Additionally, RBE is influenced by the specific type of cells or tissues being targeted. As a result, a standard RBE value cannot be uniformly applied to all patients or clinical scenarios. Accurate treatment planning requires a tailored approach to RBE estimation to account for these variables and optimize therapeutic outcomes. For these reasons, it is essential to implement a biophysical model capable of accurately and reliably calculating the biological effectiveness of radiation. For proton therapy, the use of a generic RBE value of 1.1 is currently considered appropriate in clinical settings. However, it has been observed that in the final few millimeters of the spread-out Bragg peak (SOBP), a "hot spot" may form, where the biological effectiveness can be higher. This phenomenon must be carefully considered during treatment planning, particularly when single-field techniques are employed or when the irradiation occurs near critical structures [23].In carbon ion therapy, the RBE is determined using

models. This study focuses exclusively on the Local Effect Model (LEM) version I, as it is the model employed in European facilities treating cancer patients with carbon ion beams, including the National Center for Oncological Hadrontherapy (CNAO) in Italy. The LEM aims to predict the biological impact of ion radiation based on the cellular or tissue responses to photon radiation, leveraging the extensive database accumulated from conventional radiation therapy. It relies on the concept of the "local dose," defined as the expected value of energy deposition at any point within the radiation field, given a specific pattern of particle trajectories. The central assumption of the LEM is that equal

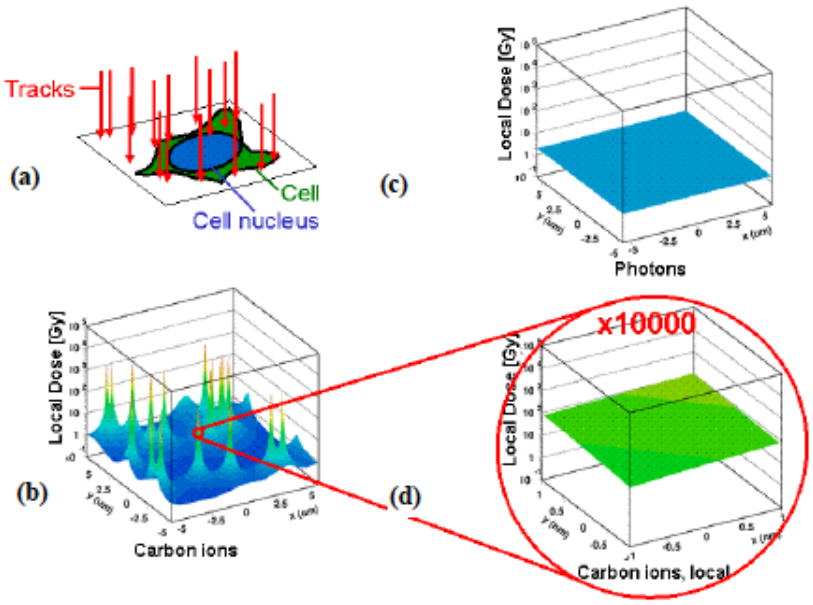

Figure 1.22: Comparison of microscopic local dose distributions for carbon ions and photons at the same macroscopic dose of 2 Gy. For a random distribution of particle tracks through a cell (a), the local dose distribution shows very high peaks near the particle trajectory (b). In contrast, photon distributions are generally uniform (c). On a nanometric scale, particle distributions can also be approximated as uniform (d), establishing a link to photon distributions [16].

local doses result in equivalent biological effects, regardless of the type of radiation. This local dose is derived from an amorphous track structure, which represents energy deposition as a function of radial distance from the particle's trajectory. The effectiveness of ion radiation is therefore calculated using the microscopic distribution of the local dose, focusing on ion tracks traversing the cell nucleus, which is considered the primary target for the radiation effects observed at the cellular level [16]. This model assumes that the critical target of the cell is uniformly distributed over the volume of the cell nucleus,V, without any variation of radiosensitivity within the nucleus or between nuclei of different cells. Figure 1.22 shows that when comparing the microscopic local dose distributions of carbon ions and photons, even when the same macroscopic dose (e.g. 2 Gy) is delivered, distinct differences emerge due to the nature of particle interactions. Carbon ions, being

high LET particles, produce random traversals through the cell, which result in intense energy deposition near the particle tracks. This localized energy deposition creates sharp, high-energy "spikes" close to the ion's trajectory, where most of the biological damage occurs due to concentrated ionization events. On the other hand, photons, which are low LET particles, exhibit a more uniform dose distribution. Their energy is spread diffusely throughout the tissue, resulting in a flatter local dose profile without such concentrated spikes of energy deposition. At the nanometer scale, the difference in dose distribution becomes even more apparent. This contrast between the two types of radiation plays a significant role in their respective biological effects, particularly in the context of radiation therapy, where carbon ions are often more effective in targeting and destroying cancer cells due to their concentrated ionization along the particle tracks.

Chapter 2

Treatment planning

Treatment planning is a critical process in radiotherapy aimed at achieving the optimal balance between delivering the therapeutic dose to the tumor and minimizing exposure to surrounding healthy tissues. The ideal objective would be to administer 100% of the prescribed dose exclusively to the target volume while avoiding any irradiation of adjacent tissues. The fundamental principle of Image-Guided Radiotherapy (IGRT) is to minimize the irradiated volume by managing tumor position and to provide optimal treatment plans based on images acquired with the patient in the treatment position prior to the session. In fact, hadron therapy typically consists of multiple sessions, or fractions, delivered over several days. However, during the course of radiotherapy, the patient's anatomy may undergo changes due to various factors, complicating the achievement of the desired treatment outcome. These factors include: physiological movements, such as respiration, intestinal peristalsis, and variations in bladder or bowel volume; tumor volume changes, for instance, tumor shrinkage as a result of ongoing therapy; and finally positioning errors, which may occur despite the use of immobilization devices. The treatment planning process in radiotherapy involves several key steps, which include:

- Acquisition of a Computed Tomography (CT) scan of the patient using an immobilization system;
- Definition and contouring of the lesion and Organs at Risk (OARs);
- Creation and optimization of the treatment plan on the CT images using the Treatment Planning System (TPS).

2.1 CT with immobilization system

The radiotherapy treatment process begins with the acquisition of a CT scan, which serves as the basis for contouring target volumes and OARs. To ensure treatment accuracy, the patient must be immobilized using a dedicated immobilization device, which plays a crucial role in minimizing both inter-fractional and intra-fractional motions. Inter-fractional motions refer to positional changes that occur between treatment sessions, while

intra-fractional motions are those occurring during the delivery of a single dose fraction. Commonly employed immobilization techniques include vacuum cushions, which conform to the patient's body shape, and thermoplastic masks, which provide a rigid support structure. These devices are specifically designed using thin, low-density materials to minimize their impact on particle range and scattering, ensuring precise dose delivery while maintaining patient comfort.

2.2 Target volume definition

The delineation and definition of Regions of Interest (ROIs) are carried out in accordance with the recommendations provided by the ICRU reports [24]. Various volumes, pertaining to both tumor and normal tissues, have been established for utilization in the treatment planning and reporting processes. The delineation of these volumes is a mandatory step in the planning process, as the absorbed dose cannot be accurately prescribed, documented, or reported without a precise specification of the target volumes and the normal tissues at risk. The volumes defined in relation to the lesion are illustrated in Figure 2.1. The first volume to be delineated is the Gross Tumor Volume (GTV), which

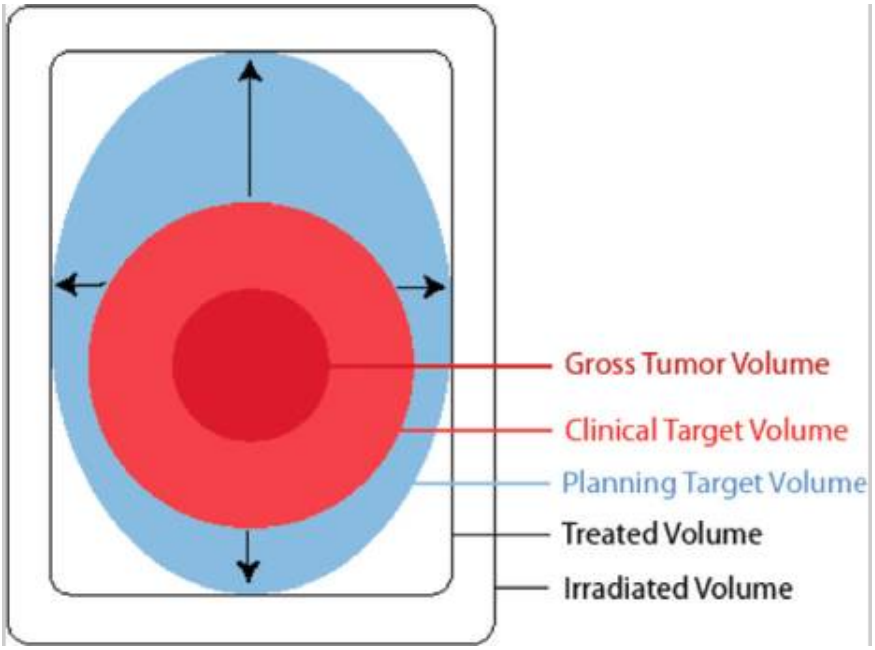

Figure 2.1: Schematic illustration of the different volumes as defined in ICRU Report 50 (1993) [25].

represents the macroscopic tumor volume. The GTV typically corresponds to the regions of malignant growth with the highest tumor cell density. Due to the elevated density of cancer cells within the GTV, it is essential to ensure the delivery of an adequate radiation dose to the entire GTV to achieve effective local tumor control in curative treatments. The second volume is the Clinical Target Volume (CTV), which encompasses the GTV and includes suspected microscopic disease that cannot be visualized with current imaging

techniques. This volume must be considered in the treatment process, and if included in the treatment plan, it should be irradiated appropriately to ensure therapeutic efficacy. The Internal Target Volume (ITV) was introduced to account for tumor position variations resulting from physiological factors. The ICRU Report 62 [26] provides guidelines on how to incorporate these uncertainties into radiotherapy planning. The ITV represents an expansion of the CTV, taking into consideration internal anatomical variations such as tumor motion due to respiration or the physiological activity of adjacent organs. The ITV is particularly beneficial in cases where tumor motion is the primary source of uncertainty, such as in lung. However, it may not be necessary when setup uncertainties predominate or are not independent of tumor motion. The ITV is considered an optional tool that can assist in the precise delineation of the Planning Target Volume (PTV). The Planning Target Volume (PTV) is a fundamental geometric concept in radiotherapy planning, as it introduces a safety margin around the Clinical Target Volume (CTV) to ensure that the delivered dose adequately covers the target volume with a clinically acceptable probability, thereby minimizing the risk of tumor underdosage. However, the precise definition of margins is crucial to avoid unnecessary irradiation of healthy tissues, thus enhancing treatment effectiveness and reducing toxicity. Furthermore, due to the limitations of irradiation techniques, the volume receiving the prescribed absorbed dose may differ from the PTV; it could be larger or smaller and generally exhibit a simpler shape. This consideration has led to the definition of the Treatment Volume (TV). The TV represents the volume of tissue encompassed within a specific isodose level, with the absorbed dose determined by the radiation oncology team as appropriate to achieve therapeutic objectives while adhering to acceptable complication thresholds. The Irradiated Volume (IV) is a concept introduced to describe the total volume of tissue that receives a significant radiation dose during radiotherapy treatment. It represents the portion of tissue receiving a dose equal to or exceeding a threshold considered clinically relevant, typically set at 50% of the prescribed dose. This volume is essential for assessing the impact of radiation on healthy tissues surrounding the tumor. The primary goal is always to minimize IV in order to reduce the risk of adverse effects while maintaining high therapeutic efficacy.

2.2.1 Organ at risk

Organs at risk (OARs) are healthy tissues located near the tumor or the irradiated area that may be susceptible to radiation-induced damage. Protecting these organs is critical to minimizing the side effects of radiotherapy. In principle, all non-target tissues could potentially be classified as OARs. However, normal tissues considered as organs at risk are typically determined based on the location of the CTV and/or the prescribed absorbed dose. From a functional perspective, tissue organization has been conceptually categorized into three types: “serial,” “parallel,” and “serial-parallel.”

- Serial organs, or organs with a serial structure (e.g., the spinal cord, nerves, and the gastrointestinal tract), consist of a chain of functional subunits, all of which are essential to maintain the overall function of the organ. Damage to even a small portion of these subunits can compromise the entire organ’s functionality;

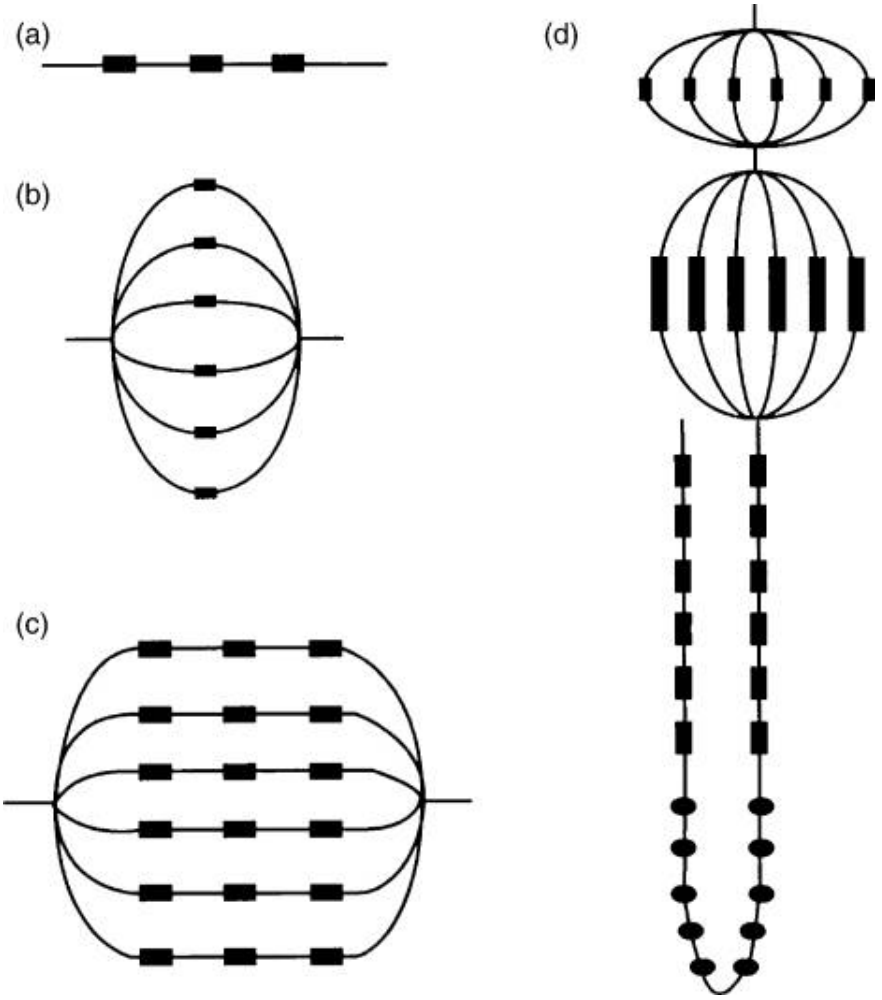

Figure 2.2: Schematic examples of tissue organization structures within the parallel-serial model: (a) a serial arrangement of subunits (e.g., the spinal cord), (b) a parallel arrangement of subunits (e.g., the lungs), (c) a serial-parallel arrangement of subunits (e.g., the heart), and (d) a combination of parallel and serial structures (e.g., a nephron) [26].

- Parallel organs, or organs with a parallel structure (e.g., the lungs and parotid glands), consist of functional subunits that operate independently of one another. For instance, in the lungs, the destruction of a limited number of alveoli does not significantly impair the overall organ function. Respiratory capacity becomes severely compromised only when a critical lung volume is damaged;
- Certain organs, such as the kidney, exhibit a mixed serial-parallel structure, incorporating both serial and parallel functional components.

The concept of tissue organization plays a crucial role in radiotherapy planning, as it enables the determination of appropriate dose-volume constraints to safeguard healthy tissues surrounding the target. Furthermore, it facilitates an accurate assessment of Dose-Volume Histograms (DVH), an essential tool for analyzing the distribution of radiation

dose within an organ or anatomical structure. For serial organs, the most reliable predictor of damage risk is the maximum absorbed dose, or the dose closest to the maximum within the irradiated volume. This is attributed to the threshold-binary response characteristic of such organs, meaning that if any part of the organ receives a dose exceeding a critical threshold, the functionality of the entire organ may be compromised. Conversely, for parallel organs, which exhibit a gradual dose-response, the most relevant parameters used to predict functional loss are the mean absorbed dose or the volume receiving a dose above a specified threshold. These measures provide a more accurate representation of the impact of radiation exposure on organ function, as the loss of a limited number of functional subunits does not significantly impair the overall organ performance, unless a critical volume is affected. The differentiation between serial and parallel organ behavior is fundamental for optimizing treatment planning, ensuring effective tumor control while minimizing the risk of radiation-induced toxicity.

2.3 Beam configuration

The definition of treatment beams is a critical phase in radiotherapy planning, as the radiation beams must be configured to ensure adequate tumor coverage while providing maximum protection to surrounding healthy tissues. Additionally, the dose delivered by the beam must be administered homogeneously. This phase requires a detailed analysis and selection of beam parameters using the TPS (Fig.2.3). The beam entry fields are cho-

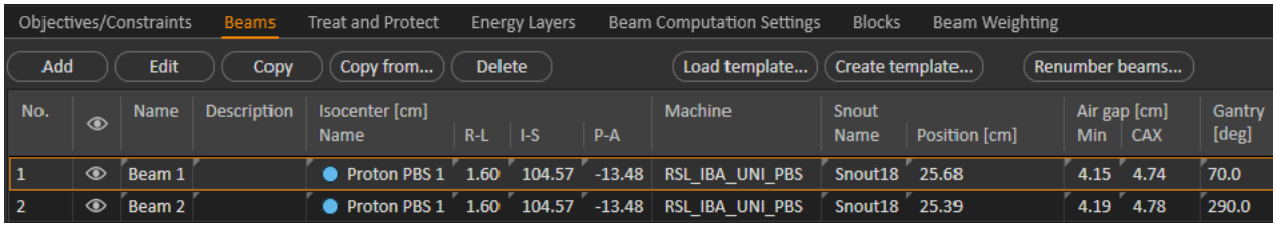

Figure 2.3: The Beams tab in the proton workspace from TPS.

sen to maximize dose delivery to the target volume while minimizing exposure to healthy tissues. Beam angles and paths are carefully evaluated to avoid critical structures and enhance the robustness of the plan, particularly in hadron therapy. In the case of proton or heavy ion beams, which are characterized by the Bragg peak, the dose is primarily confined to the target volume, significantly reducing exposure to deeper tissues (exit dose). However, if a critical structure is located immediately beyond the target, careful planning is required to minimize potential irradiation, as the sensitivity to range uncertainties and the high ballistic precision of particle therapy can lead to unintended overdose in healthy structures positioned near the target. In such cases, beam angles must be chosen to minimize the exposure of healthy organs while ensuring optimal target coverage. Furthermore, adopting a multi-field approach is advantageous as it allows for better dose conformity to the target. If distal OARs cannot be entirely avoided, distributing the dose across multiple beams ensures that no single beam causes an overdosage. An additional complexity arises from tissue heterogeneity. Areas of the body with significant variability in tissue

density, such as the air-tissue interface (e.g., lungs) or regions with high atomic number materials (e.g., bones), can influence the beam's path and energy. In particular, density variations perpendicular to the beam direction (e.g., transitions between lung tissue and ribs) should be avoided by making adjustments to the beam setup. This meticulous planning ensures the balance between effective tumor targeting and minimizing the risk to healthy tissues, addressing both anatomical and physical challenges in radiotherapy.

2.4 Dose calculation and optimization

Another crucial aspect in the development of the treatment plan is dose calculation and optimization. Dose objectives and constraints are set for each Region of Interest (ROI) through the Objectives/Constraints tab in the TPS (Fig.2.4). Focusing on inverse treatment planning, this approach employs a computational algorithm to convert treatment objectives, typically defined in the dose domain, into treatment parameters associated with the delivery system. Inverse treatment planning problems are formulated as optimization problems and are solved iteratively to achieve the desired dose distribution. The

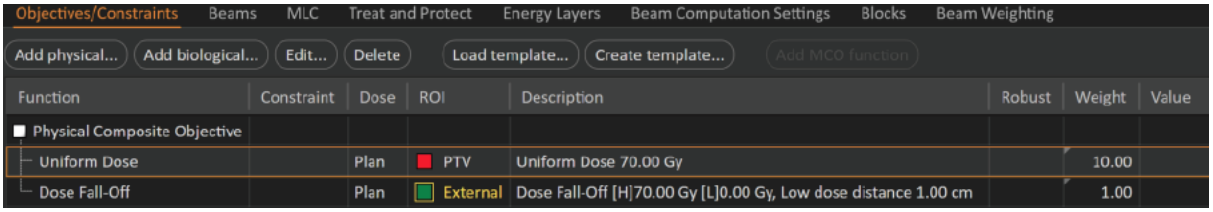

Figure 2.4: The objectives and constraints tab from TPS.

optimization algorithm works to minimize the global objective function, which consists of multiple optimization functions. It is possible to define optimization functions, which can either be integrated into the objective function or used as independent constraints. The optimization functions included in the objective function are assigned weights that reflect their relative importance (see Fig.2.5). Among the optimization functions used in the objective function, the following are commonly applied:

- Maximization of PTV coverage: the algorithm ensures that at least 95% of the PTV receives the prescribed dose;
- Minimization of dose to OARs: the algorithm seeks to limit the dose to organs at risk below a predefined safety threshold;
- Minimization of dose heterogeneity: prevents significant dose variations within the PTV, thereby reducing the risk of damage to surrounding healthy tissues.

In addition to the optimization objectives, certain mandatory conditions must be satisfied regardless of the objective function's optimization. These are constraints, which limit the range of possible solutions to ensure the treatment plan remains clinically acceptable. Among the optimization functions used as constraints, the most relevant include:

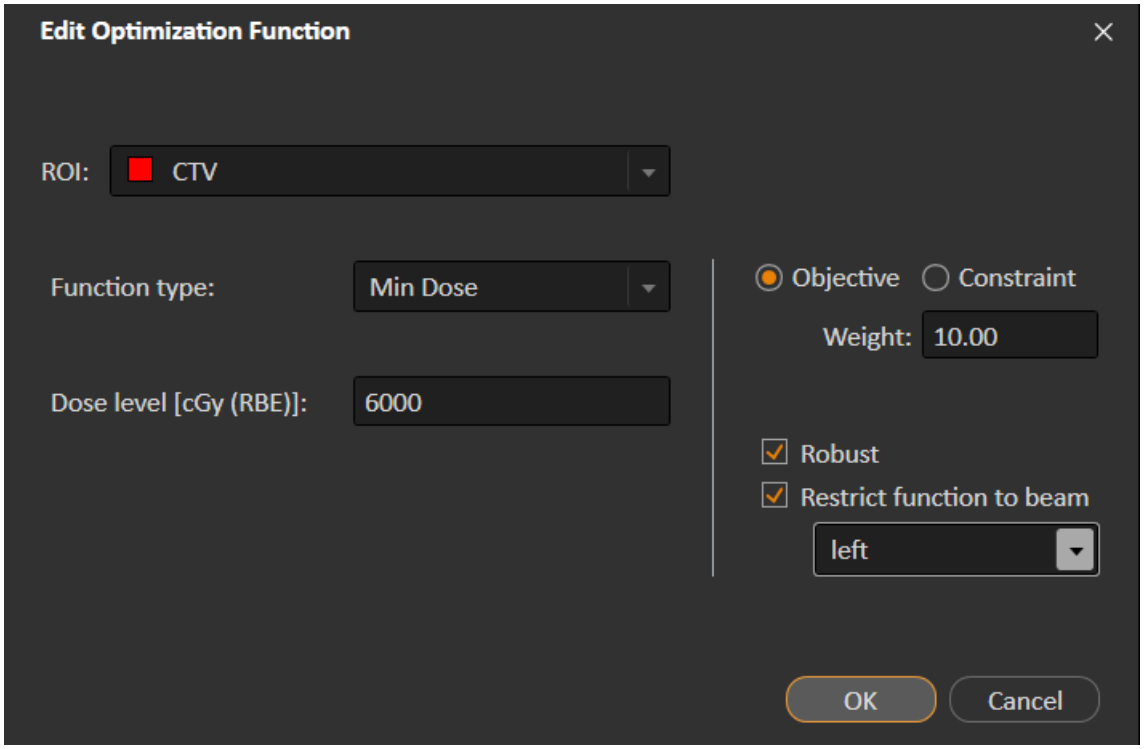

Figure 2.5: The Add Optimization Function dialog from TPS.

- Maximum dose to OARs: ensures that the dose to critical structures does not exceed a specified threshold;

- Dose conformity to the PTV: the volume of the PTV receiving less than 95% of the prescribed dose must be below 5% of the total PTV volume;

- Steep dose gradients at the transitions between the PTV and OAR: the optimization algorithm must ensure a rapid dose fall-off in critical organs to minimize damage to healthy tissues.

The optimal solution is the one that provides the best value of the objective function while ensuring that no constraints are violated, thereby achieving a clinically acceptable and effective treatment plan. Target coverage and the dose received by OARs are assessed using DVHs (Fig.2.6). The most commonly used DVH in clinical practice is the cumulative DVH, which represents the volume of a structure receiving at least a specified dose. The DVH provides essential information on the dose distribution within a structure and the homogeneity of the dose delivery, which can be evaluated based on the steepness of the curve. However, the DVH does not indicate the spatial location of high- or low-dose regions within the structure. Therefore, it is always beneficial to complement DVH analysis with isodose charts, which offer a spatial representation of the dose distribution.

Figure 2.6: The Dose-Volume Histograms for different ROIs.

2.5 Robust radiotherapy optimization

Robust optimization is an advanced technique used in radiotherapy treatment planning to ensure that the dose distribution remains effective despite uncertainties and variations that may occur during treatment. As previously explained, these uncertainties may arise from setup errors, anatomical and physiological variations in the patient, or inaccuracies in the estimation of particle range in hadron therapy. Robust optimization is based on the simulation of multiple error scenarios during the planning process. In the TPS, the user specifies uncertainty values for the following factors (Fig.2.7):

- Setup errors (patient shifts, e.g., ±3 mm);
- Range errors (variations in tissue density, e.g., ±3.5%);
- Organ motion (incorporation of multiple CT scans acquired at different time points, e.g., inspiratory and expiratory phases for lung treatments).

The system generates multiple error scenarios, each representing a possible real configuration of the patient during treatment. Robust optimization aims to minimize the worst objective function value across all scenarios, ensuring that the treatment plan remains effective even under the most unfavorable conditions. This approach is known as min-max optimization. Robust optimization is particularly beneficial in proton therapy and heavy ion therapy, where small errors can have a significant impact on the quality and effectiveness of the treatment because the high ballistic precision of the Bragg peak makes

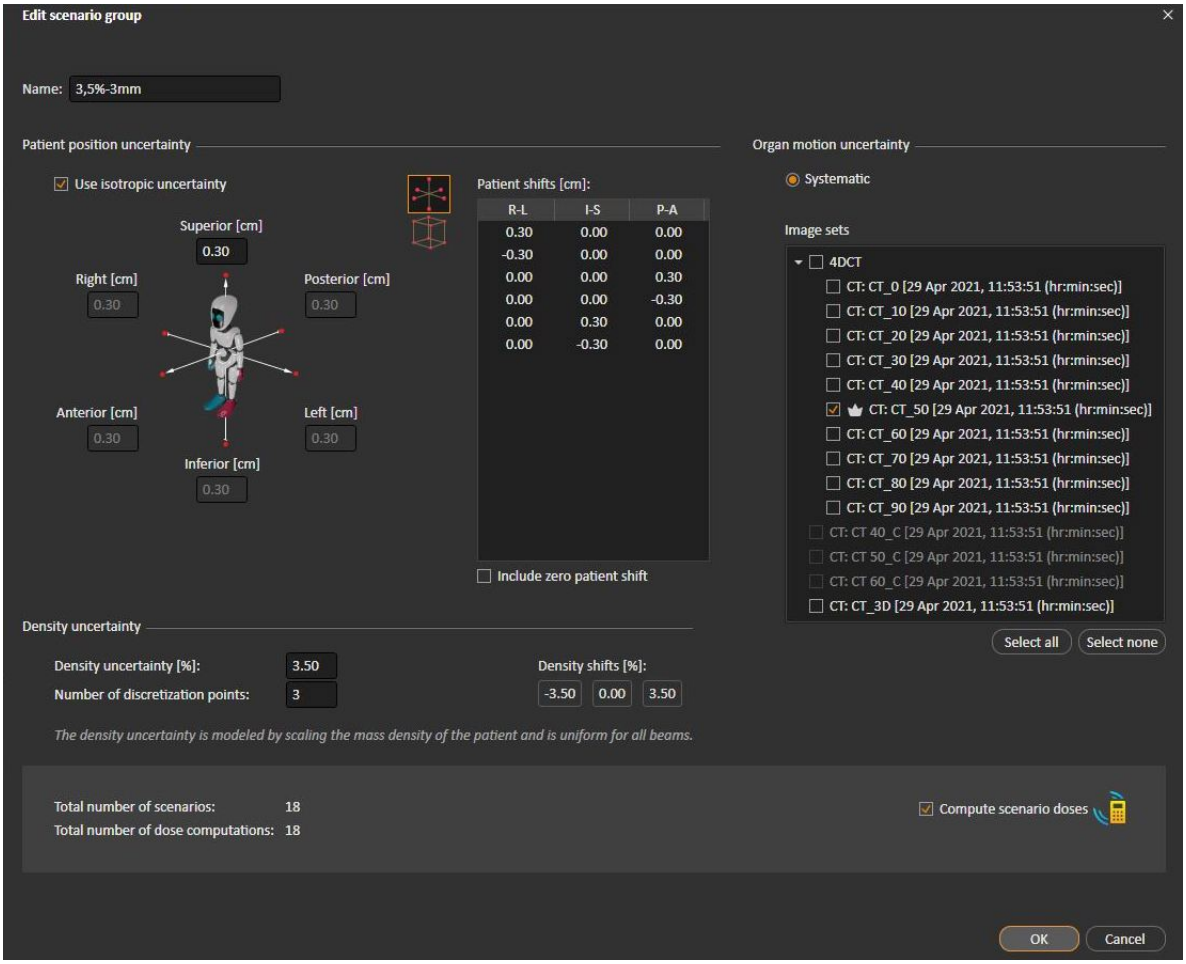

Figure 2.7: RayStation interface showing the parameter settings used to generate the 18 dose scenarios required for the robustness evaluation in Chapter 4.

it highly sensitive to uncertainties and variations in the densities of the traversed tissues, unlike photon-based treatments.

2.6 Stereotactic body radiation therapy (SBRT)

After outlining the fundamental principles and key steps in the development of a radiotherapy treatment plan, this section introduces Stereotactic Body Radiotherapy (SBRT) as a specific technique. In particular, the focus will be on SBRT applied to pulmonary lesions, which is one of the subjects explored in this thesis and will be discussed in the following chapter. SBRT is a highly precise radiotherapy technique in which accurate target localization, combined with a high dose per fraction, is utilized to treat specific tumors. The term "stereotactic" in this context refers to the target-centric nature of SBRT, where typically small treatment volumes, narrow margins, and steep dose gradients are used to achieve a highly conformal high-dose distribution over a small region, with the delivery of a high dose per fraction. SBRT targets are typically small, which minimizes

dose-volume-related adverse effects on surrounding healthy tissues. This advanced technology demands a high level of precision, accuracy, and reproducibility throughout the entire treatment delivery process. The main characteristics of SBRT dose distribution include:

- Steep dose gradients at the interface between the target and adjacent healthy tissues;
- High dose conformity to the tumor volume;

To safely deliver high doses to the target, ensuring precise tumor localization is of paramount importance. Due to its intrinsic characteristics, lung SBRT requires highly reproducible methodologies to achieve precise treatment setups while accounting for and mitigating respiratory motion effects. Ensuring optimal patient positioning during dose delivery necessitates a robust immobilization system capable of maintaining the patient in a stable and consistent position throughout the entire treatment session. The subsequent step in patient simulation for lung SBRT involves incorporating tumor and organ motion into the treatment planning process. Strategies to manage respiratory motion can be broadly categorized into three approaches: restriction, gating, and tracking [27]. SBRT entails greater risks compared to other radiotherapy techniques due to the high dose per fraction. For this reason, the use of advanced techniques such as respiratory gating, breath-hold, abdominal compression, and real-time tumor tracking is particularly beneficial for these treatments. These methodologies leverage additional technologies to minimize irradiation to the surrounding healthy tissues.
One of the most common solutions for managing respiratory motion is respiratory gating, which utilizes an activation signal to control the delivery of radiotherapy. In this thesis project, the gating technique was employed for the development of SBRT lung treatment plans. This means that the radiation beam is switched on only when the target is within a specific region, thereby reducing the total irradiated volume. Using four-dimensional computed tomography (4D-CT), imaging data are acquired throughout the respiratory cycle and sorted based on either breathing amplitude or respiratory phase (where 0% phase corresponds to maximum inhalation and 50% phase corresponds to maximum exhalation). The result is a series of images that represent the position of the target at different points in the respiratory cycle (see Figure 2.8). The target and surrounding organs were contoured at the respiratory phases selected for gating. To enhance the robustness of motion management, the ITV is constructed, as previously introduced in Section 2.2. In the treatment plans presented in the following chapter, the ITV was generated as a convolution of the CTV over three consecutive respiratory phases (Figure 2.9). This method helps to reduce uncertainties and maintain a more confined ITV, thereby avoiding overestimation of the irradiated area. Although respiratory gating offers several advantages over other motion management strategies, such as allowing the patient to breathe freely, improving accessibility, and enhancing patient comfort, it also presents challenges that require a high level of technical expertise. In particular, the selection of the gating window must carefully balance the reduction of normal tissue irradiation with the increase in treatment time. Additionally, the practical implementation of gating has certain limitations, including: prolonged treatment times, as the beam remains active

only for a fraction of the total respiratory cycle; imperfect correlation between the external respiratory signal and the actual internal tumor motion, which may affect gating accuracy; and respiratory irregularities, which can hinder the reproducibility of gating across different treatment sessions.

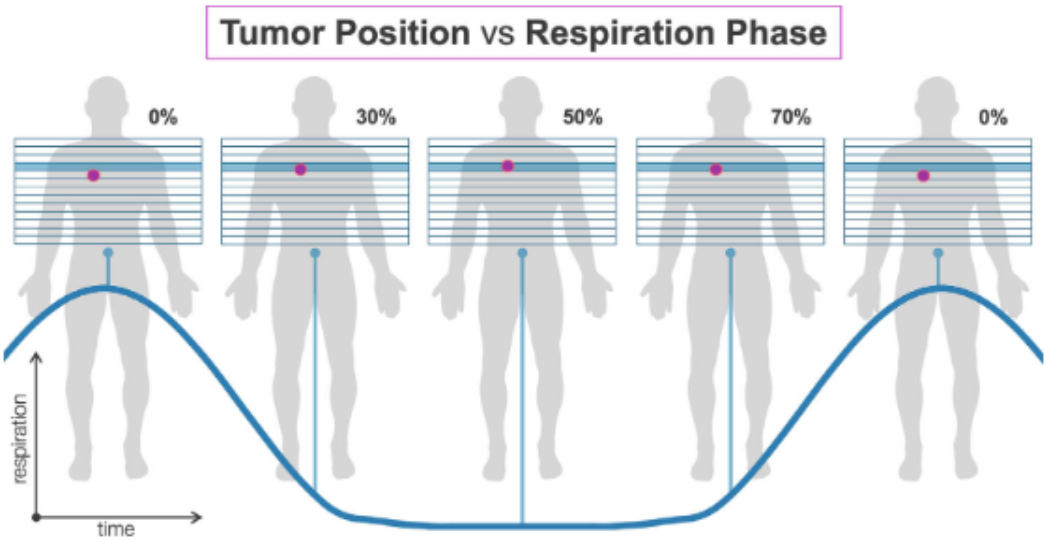

Figure 2.8: Illustration of tumor position across different phases of the respiratory cycle, along with the corresponding amplitude of the respiratory trace [28].

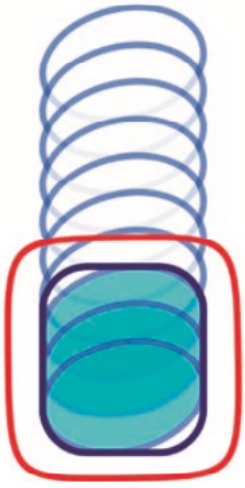

Figure 2.9: Schematic illustrating the gating technique for motion management. The ellipse shape depicts tumor target motion over breathing phases; the smaller rectangle depicts the ITV, and the larger rectangle depicts the beam aperture [29].

Chapter 3

In silico comparison study

A dataset of 20 4DCT DICOM scans from patients with peripherally located pulmonary lesions was selected for this in silico study. The study aimed to perform a comparative treatment analysis to evaluate proton, carbon ion and photon radiotherapy plans.
The photon-based treatment plans were optimized by the Medical Physics Unit of Fondazione IRCCS San Gerardo dei Tintori (Monza), whereas the proton and carbon-ion treatment plans were developed as part of this thesis project at CNAO in Pavia. The 20 patients included in this study received different dose prescriptions depending on the anatomical characteristics of the lesion (see Table 3.1). The prescribed dose regimens were as follows: 60 Gy in 8 fractions (25% of cases); 48 Gy in 4 fractions (20% of cases); and 50 Gy in 5 fractions (55% of cases). The CTV in the analyzed dataset ranges from 0.4 cm^3 to 37.4 cm^3. As previously mentioned, all lesions included in this study are peripherally located, making the analysis particularly relevant for assessing the potential toxicity associated with SBRT. Specifically, this study aims to compare the three treatment modalities based on target coverage and organ sparing, in order to determine which approach provides the most effective dose distribution while minimizing radiation-induced toxicity. Particular attention is given to the risk of radiation pneumonitis and rib fractures, assessing which modality offers superior protection to healthy tissues. The planning objectives were defined prior to the development of the treatment plans and were consistently applied across all cases. The coverage objective required that at least 95% of the CTV receive 100% of the prescription dose. To prevent overdose, it was also required that the CTV volume receiving 107% of the prescription dose be less than 5%. Furthermore, the maximum dose (D_{max}) was set at 110% of the prescription dose, and this dose level had to remain confined to a volume smaller than 0.1 cc [1]. Similarly, OAR constraints were established a priori, prior to treatment plan optimization. Table 3.2 summarizes the dose constraints for OARs, differentiated according to the fractionation schedule specified in the prescription.

[1]The term "cc" stands for cubic centimeter, a unit of volume commonly used in dosimetry to quantify the volume of tissue receiving a specific radiation dose.

Table 3.1: Dose prescription details for each patient, including fractionation and lesion location. The table reports the prescribed dose per fraction (D/fx, in Gy [RBE]), the number of fractions (fx), and the total prescribed dose (D, in Gy [RBE]) for each patient undergoing radiotherapy. The final column specifies the anatomical location of the lesion within the lungs.

	Prescription			**Lesion location**
Patient	**D/fx Gy[RBE]**	**fx**	**D Gy[RBE]**	
LUNG_01	7.5	8	60	Right inferior lobe
LUNG_02	10	5	50	Left superior lobe
LUNG_03	12	4	48	Right superior lobe
LUNG_04	10	5	50	Left superior lobe
LUNG_05	10	5	50	Left inferior lobe
LUNG_06	10	5	50	Right superior lobe
LUNG_07	10	5	50	Right superior lobe
LUNG_08	12	4	48	Left lung
LUNG_09	10	5	50	Right lung apex
LUNG_10	7.5	8	60	Right superior lobe
LUNG_11	12	4	48	Left lung
LUNG_12	12	4	48	Right lung
LUNG_13	7.5	8	60	Right lung
LUNG_14	7.5	8	60	Right superior lobe
LUNG_15	7.5	8	60	Right superior lobe
LUNG_16	10	5	50	Right superior lobe
LUNG_17	10	5	50	Left superior lobe
LUNG_18	10	5	50	Left superior lobe
LUNG_19	10	5	50	Right superior lobe
LUNG_20	10	5	50	Right inferior lobe

It is important to note that, while all standard OAR constraints for lung treatments are reported, from this point onward, the analysis will focus on a subset of OARs (specifically the ribs, chest wall, and lungs-ITV) due to the peripheral location of the lung lesions treated in this study. This decision is supported by several studies ([30] ,[31]) that highlight the clinical relevance of these structures in terms of SBRT associated toxicity.

Table 3.2: Dose constraints for OARs across different fractionation schedules. The table presents the maximum allowable dose thresholds for each organ at different fractionation regimens.

Organs	**12 Gy[RBE] × 4**	**10 Gy[RBE] × 5**	**7.5 Gy[RBE] × 8**
Chest Wall*	$D_{70cc} < 16.2$	$D_{70cc} < 17.6$	$D_{70cc} < 20.6$
	$D_{2cc} < 42$	$D_{2cc} < 50$	$D_{2cc} < 61.1$
Ribs	$D_{2cc} < 30.7$	$D_{2cc} < 33.7$	$D_{2cc} < 40.6$
Lungs-ITV	$V_{20Gy} < 10\%$	$V_{21.8Gy} < 10\%$	$V_{25.8Gy} < 10\%$
	$D_{1500cc} < 11.6$	$D_{1500cc} < 12.5$	$D_{1500cc} < 14.3$
	$D_{1000cc} < 12.4$	$D_{1000cc} < 13.3$	$D_{1000cc} < 15.3$
Spinal Cord	$D_{1cc} < 13.6$	$D_{1cc} < 14.8$	$D_{1cc} < 17.5$
	$D_{0.1cc} < 18.3$	$D_{0.1cc} < 20.2$	$D_{0.1cc} < 24$
	$D_{0.035cc} < 21$	$D_{0.035cc} < 23$	$D_{0.035cc} < 27.8$
Esophagus	$D_{5cc} < 18.8$	$D_{5cc} < 20.4$	$D_{5cc} < 24$
	$D_{1cc} < 23$	$D_{1cc} < 25.1$	$D_{1cc} < 29.9$
	$D_{0.035cc} < 30$	$D_{0.035cc} < 32.9$	$D_{0.035cc} < 39.6$
Heart	$D_{15cc} < 28$	$D_{15cc} < 30.7$	$D_{15cc} < 36.9$
	$D_{0.035cc} < 34$	$D_{0.035cc} < 37.3$	$D_{0.035cc} < 45.1$
	$D_{4cc} < 15.6$	$D_{4cc} < 16.9$	$D_{4cc} < 19.7$
Trachea and Bronchi	$D_{0.035cc} < 34.8$	$D_{0.035cc} < 38.2$	$D_{0.035cc} < 46.3$

* The chest wall is defined as the soft tissue structure including intercostal muscles and excluding lung volume, mediastinal soft tissue, and anterior vertebral body. The ribs are contoured by outlining the bone, ensuring that adjacent ribs are not contoured as a single continuous structure, i.e., excluding the intercostal spaces. *Abbreviations:* D_{xcc}, the dose to x cm^3 of the volume; V_{xGy}, the percentage volume covered by the x Gy (RBE) isodose line.

3.1 Photon volumetric modulated arc therapy (VMAT) plans

The photon treatment plans, developed by the Medical Physics Unit of Fondazione San Gerardo, were created using Volumetric-Modulated Arc Therapy (VMAT). This technique is a form of arc therapy in which the dose is delivered through a continuous rotation of the gantry, the radiation source, allowing the patient to be treated with a full 360° beam angle. To manage respiratory motion, the respiratory gating technique was employed. The ITV was defined as the convolution of the CTV in the two respiratory phases closest to the maximum inhale phase. Referring to the representation of the respiratory cycle in Fig.2.8, the CT_0, CT_10, and CT_80 scans were selected for ITV construction. Specifically:

- CT_0 corresponds to the maximum inhale phase.
- CT_10 and CT_80 represent the two contiguous respiratory phases adjacent to CT_0, selected to ensure a more robust ITV definition.

The respiratory-gated VMAT treatment plans were optimized on a PTV, which was derived by applying a 3 mm isotropic expansion to the ITV to account for setup uncertainties and residual motion. Optimization was performed using the Monaco TPS, specifically tailored for VMAT planning. Treatment delivery was designed for the Elekta Versa HD linear accelerator, operating with 6 MV Flattening Filter Free (FFF) photon beams. The system is equipped with a 160-leaf Multi-Leaf Collimator (MLC), featuring 5 mm leaf thickness at the isocenter, allowing for precise modulation of dose distribution. The treatment delivery utilized two coplanar partial arcs.

3.2 Intensity modulated proton therapy (IMPT) plans

Intensity-Modulated Proton Therapy (IMPT) is an advanced form of proton beam therapy that enables highly conformal dose distributions while minimizing radiation exposure to surrounding healthy tissues. The IMPT plans developed in this project at CNAO utilize an active scanning beam system for particle therapy delivery (Fig.3.1). This approach involves dividing the tumor volume into slices, which are oriented orthogonally to the particle beam direction and correspond to different energy levels of the beam. The irradiation

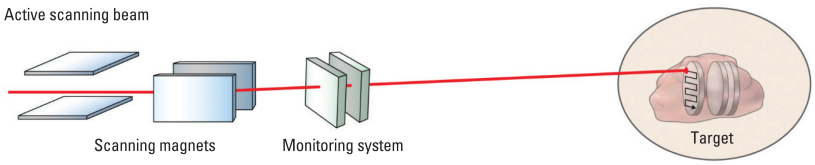

Figure 3.1: Schematic representations of active scanning beam delivery systems utilized in particle therapy [32].

process is carried out through the superposition of a sequence of microbeams (beamlets),

each delivering a predefined number of particles to a specific irradiation point, referred to as a spot. The set of spots forms a grid, where each grid point represents a unique combination of beam energy, transverse position, and number of prescribed ions. The position of the Bragg peak is controlled by adjusting the beam energy or by modifying beam penetration using passive absorbers such as range shifters, enabling layer-by-layer dose painting to achieve precise dose deposition. To further enhance dose conformity, Multifield Optimization (MFO-IMPT) is implemented. This technique allows for the simultaneous modulation of all treatment fields, improving dose homogeneity and OARs sparing. For each patient, two to four coplanar fields with fixed angles were used, meaning that multiple beam entry directions were chosen while remaining within the same geometric plane. The gantry angles varied to optimize dose distribution, but no non-coplanar beams were included.
Similarly to VMAT plans, a respiratory-gated technique was employed for IMPT planning. The $ITV_{40-50-60}$ was defined as the convolution of the CTV over the two contiguous respiratory phases closest to the maximum exhalation phase (CT_50). Specifically, the CT_50 scan corresponds to the maximum exhalation phase, while the CT_40 and CT_60 scans represent the adjacent respiratory phases. These were selected to ensure a more robust definition of the ITV, reducing uncertainties in target delineation due to respiratory motion. To ensure treatment robustness, all IMPT plans were optimized on the CTV using robust optimization techniques that accounted for 3 mm isotropic shifts and a 3.5% density uncertainty scenario. The optimization process was performed using the RayStation TPS (RaySearch, Sweden) in conjunction with the ProBeat Proton Therapy delivery system (Hitachi, Japan).

3.2.0.0.1 Collimator aperture configuration: As detailed in the introductory chapter, proton therapy offers a significant advantage over photon-based radiotherapy due to the physical phenomenon of the Bragg Peak, which allows for a highly localized dose deposition within the tumor while substantially reducing exposure to healthy tissues beyond the target. Additionally, proton therapy significantly reduces the entrance dose compared to photon-based treatments, further minimizing unnecessary irradiation to healthy tissues. However, one of the primary limitations of this technique is the lateral dose distribution. To mitigate this issue, and in accordance with previous studies ([33], [34]), this project aimed to develop hybrid treatment plans that combine the active spot-scanning technique with the use of a collimator. The planning and optimization process began with the creation of 20 IMPT plans, one for each patient, without collimation. Subsequently, three additional configurations were explored, generating 20 IMPT plans for each collimator aperture size: 3 mm, 4 mm, and 5 mm. The treatment plans were evaluated and compared based on key dosimetric indices, including the homogeneity index (HI), conformity index (CI), and gradient index (GI), as well as CTV coverage.
Various definitions of dosimetric indices related to coverage, homogeneity, conformity, and gradient have been proposed in the literature to assess the quality of treatment plans. In this study, we followed the recommendations of Yaparpalvi et al.[35], which suggest the following metrics as appropriate surrogates for establishing quality guidelines for lung

SBRT treatment planning. Homogeneity index defined according to ICRU 83 [43] as:

$$HI_{\text{ICRU 83}} = \frac{D_{2\%} - D_{98\%}}{D_{50\%}} \tag{3.1}$$

where $D_{2\%}$ is the near-maximum dose, i.e., the dose received by 2% of the target volume,$D_{98\%}$ is the near-minimum dose, i.e., the dose received by 98% of the target volume,$D_{50\%}$ is the median dose within the target. The HI quantifies the range between the near-maximum and near-minimum doses, normalized to the median dose. The ideal value, corresponding to a perfectly uniform dose distribution within the target, is HI = 0. Conformity Index (CI) defined according to Paddick et al. [37] as:

$$CI_{\text{Paddick}} = \frac{(TV \cap PIV)^2}{TV \times PIV} \tag{3.2}$$

where TV refers to $ITV_{40-50-60}$ (for particle therapy plans) or PTV (for photon therapy plans), PIV is the prescription isodose volume, $TV \cap PIV$ is the intersection between the target volume and the prescription isodose volume. The CI assesses how well the prescribed dose distribution conforms to the target volume. The ideal value is CI = 1, which occurs when the volume receiving the prescribed dose exactly matches the target volume. Gradient Index (GI) is defined according to RTOG 0915 protocol as:

$$GI = R_{50\%} = \frac{PIV_{50\%}}{PTV} \tag{3.3}$$

where $PIV_{50\%}$ is the volume of the 50% prescription isodose, PTV is the planning target volume. This metric evaluates low-dose spillage, indicating how much the volume irradiated to 50% of the prescription dose extends beyond the PTV. A lower $R_{50\%}$ value corresponds to a steeper dose fall-off outside the target, signifying better dose conformity and reduced irradiation of surrounding healthy tissues. The box plots of dosimetric indices and CTV coverage across different collimator configurations are summarized in Figure3.2. Regarding the HI, the collimator configuration with a 3 mm aperture exhibits a wider distribution compared to the other configurations, with a slightly higher median value. These results suggests that this configuration may not be the optimal choice for ensuring a uniform dose distribution. The 4 mm and 5 mm collimators appear to provide the best compromise between good dose homogeneity and reduced variability across treatment plans. Additionally, the 5 mm configuration presents slightly lower values compared to the 4 mm configuration. The no-collimator configuration displays the lowest median values among all configurations. However, the reduction in HI observed in the absence of a collimator may be attributed to increased lateral dose dispersion, which promotes a more uniform distribution within the target but may compromise dose selectivity. Indeed, referring to the CI, the no-collimator configuration exhibits the poorest performance, with a lower median value and high variability, indicating reduced dose conformity to the target. Among the collimator configurations, the median CI for the 5 mm collimator is comparable to those of the 3 mm and 4 mm configurations, confirming that it provides good dose conformity. While the 4 mm collimator exhibits the lowest variability, the 5 mm configuration still maintains an acceptable dispersion, ensuring a predictable and reliable

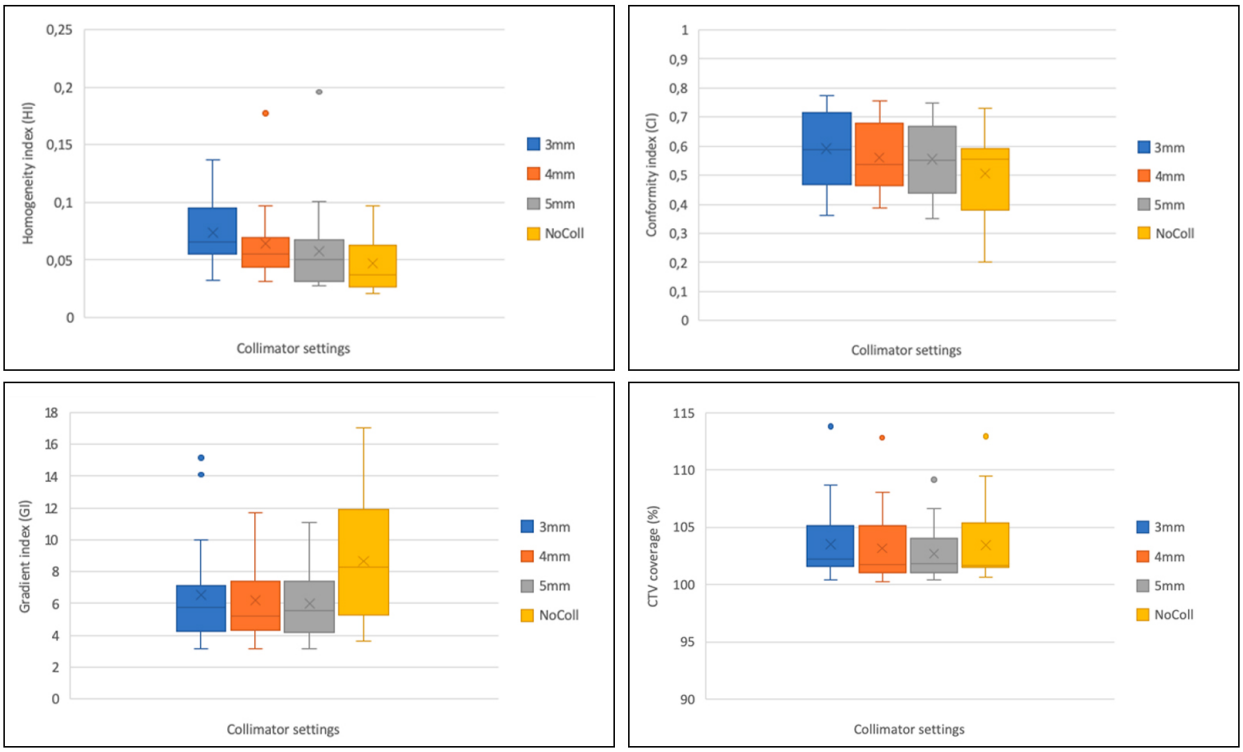

Figure 3.2: Box plots comparing key dosimetric indices across different collimator configurations (3 mm, 4 mm, 5 mm, and NoColl). The top-left plot shows the Homogeneity Index (HI), where lower values indicate greater dose uniformity. The top-right plot represents the Conformity Index (CI), with values approaching 1 suggesting better dose conformity to the target. The bottom-left plot illustrates the Gradient Index (GI), where lower values indicate a steeper dose fall-off outside the target. The bottom-right plot displays CTV coverage (%). The boxes extend from the first quartile (Q1) to the third quartile (Q3), with the central line representing the median value. The whiskers indicate the smallest and largest values. The cross represents the mean value.

CI across different treatment plans. Additionally, the 5 mm collimator may contribute to improved treatment efficiency, potentially reducing beam-on time without compromising dose conformity. This makes it a favorable choice in a clinical setting where both dose precision and practical treatment delivery are crucial. Finally, regarding the GI, the presence of a collimator further confirms an improvement in treatment plans. Specifically, a lower GI is observed for the 3 mm, 4 mm, and 5 mm collimator configurations compared to the no-collimator configuration, which suggests a less effective dose fall-off beyond the target. The 3 mm collimator appears to provide the greatest reduction in GI; however, the presence of some outliers with higher values than the group mean may indicate increased variability in certain cases. The interquartile range (IQR) for the 5 mm configuration is comparable to that of the 3 mm and 4 mm configurations. Nevertheless, considering the additional information from other dosimetric indices, the 5 mm configuration represents

a well-balanced option, offering a controlled GI while maintaining acceptable variability. To determine the optimal collimator configuration for CTV coverage, the coverage values were normalized to the prescribed dose to account for variability due to different fractionation schemes. In addition to assess treatment plans that met the coverage prescription ($V_{100\%} \leq 95\%$), compliance with the maximum dose constraint ($D_{0.1cc} \leq 110\%$) was also verified. The box plot for CTV coverage shows that all configurations exhibit a similar median, approximately 100% CTV coverage, indicating that each configuration ensures adequate dose coverage. The 5 mm collimator presents a more compact distribution, with a reduced interquartile range (IQR) compared to the 3 mm, 4 mm, and NoColl configurations. Conversely, the NoColl configuration exhibits the widest data dispersion, suggesting increased variability in dose distribution. Moreover, the 3 mm, 4 mm, and NoColl configurations contain outliers exceeding 110% of the prescribed dose, indicating that in some treatment plans, the delivered dose surpasses the maximum dose constraint. Thus, the choice of the 5 mm collimator is justified as it provides: adequate CTV coverage, more controlled and less variable dose distribution (reduced IQR), and lower risk of overdose occurrences.

3.3 Carbon ion radiotherapy (CIRT) plans

The planning of Carbon Ion radiotherapy (CIRT) at CNAO follows a methodology similar to that of CIRT, utilizing an active scanning beam system (Fig.3.1) to ensure precise dose delivery. Unlike proton therapy, which can be administered using a rotating gantry, carbon ion treatments at CNAO are delivered through fixed horizontal or vertical beams. In this configuration, treatment plans were developed using two or more coplanar static fields or a multifield setup with three non-coplanar fields, aiming to optimize target coverage and spare OARs
Similar to IMPT, a respiratory motion management strategy was implemented using respiratory gating. The ITV was defined by convolving the CTV over the two contiguous respiratory phases closest to maximum exhalation (CT_50), specifically CT_40 and CT_60, ensuring robust target delineation while accounting for respiratory motion uncertainties. The robust optimization process for CIRT was performed using the RayStation TPS(RaySearch, Sweden), considering 3 mm isotropic shifts and a 3.5% density uncertainty, to enhance the robustness of the treatment plans. Unlike other delivery techniques that employ patient-specific collimators, carbon ion beams at CNAO were not collimated using a mechanical collimation system. Instead, lateral dose shaping was achieved exclusively through active spot-scanning and robust optimization, ensuring precise dose modulation.

It is important to emphasize that the generation of a radiotherapy treatment plan involves several key steps, requiring continuous interaction between the medical physicist, radiation oncologist, and TPS. Once the imaging data is acquired, the radiation oncologist delineates the target volumes (CTV, ITV) and the OARs, and defines the clinical prescription (e.g., dose, fractionation, and constraints).
Subsequently, the medical physicist configures the beam parameters (e.g., angles, energy,

collimation, and range shifters for particle therapy) and initiates the optimization within the TPS. Although the TPS performs the actual dose optimization based on the objective functions, the process is iterative and requires several rounds of manual refinement, especially when multiple trade-offs are involved (e.g., target coverage vs. OAR sparing). Depending on the complexity of the case and the technique used, the time required to produce a clinically acceptable plan can range from 2 to 8 hours per plan.
In this study, the optimization of each plan was performed manually, including beam setup, robustness settings, and objective tuning. For each of the 20 patients, four proton plans were generated with different collimator settings (NoColl, 3 mm, 4 mm, and 5 mm), along with one carbon ion plan, leading to a total of 100 plans. This considerable planning effort, encompassing beam definition, parameter tuning, and quality assurance for each case, reflects not only the complexity of particle therapy planning but also the extensive workload carried out during this thesis project.

Chapter 4

Plan evaluation and comparison

The evaluation of a radiation therapy treatment plan represents a fundamental step in verifying that the selected modality ensures optimal therapeutic efficacy while minimizing toxicity to healthy tissues. In this chapter, the methodology used to assess and compare the treatment plans is presented. When dealing with particle therapy, the concept of RBE must be considered, as the biological impact of the same physical dose varies depending on the radiation type. In the case of proton therapy (IMPT), a constant RBE of 1.1 is assumed, meaning that the reported dose in Gray (Gy) is already adjusted to reflect the expected biological effect. For carbon ion radiotherapy (CIRT), where the biological effectiveness is strongly dependent on factors such as LET and tissue type, the Local Effect Model I (LEM1) [39] is used to compute the RBE-weighted dose (Gy(RBE)), providing a more refined estimation of the therapeutic effect. The RBE corrections for both IMPT and CIRT were incorporated directly during the optimization process in RayStation TPS. Conversely, photon-based VMAT plans are optimized and evaluated purely in terms of physical dose (Gy), without the need for RBE corrections. This fundamental difference in dose representation makes direct dosimetric comparison between modalities non-trivial.
A critical aspect of this comparison concerns the fractionation schedules used for carbon ion plans. Currently, only a limited number of SBRT protocols for CIRT in lung tumors are available in the literature [38]. However, specific dose constraints for carbon ion therapy are not explicitly reported in these studies. As a result, the same fractionation schemes used for IMPT and VMAT were adopted in this work for CIRT, despite the awareness that this choice may not be fully optimal for carbon ion therapy. This decision was made to ensure that all treatment plans remained comparable under the same fractionation conditions, allowing for a more consistent evaluation across modalities. Since the analyzed treatment plans involve three different fractionation schedules, a direct comparison of prescribed doses in Gy or Gy(RBE) would not be appropriate. For this reason, OARs constraints (Table 4.1), originally reported in Table 3.2, are now expressed in terms of BED (see Eq.(1.31)), ensuring a consistent radiobiological framework across different fractionation schemes.

The comparison of these plans is based on multiple evaluation criteria, grouped into

three main categories:

- Dosimetric Evaluation: analysis of dose distribution within the target volume and healthy tissues, including coverage of the CTV and OARs constraints expressed in BED;
- Robust Evaluation: assessment of the sensitivity of each treatment modality to setup and range uncertainties, particularly relevant for proton and carbon ion therapy;
- Radiobiological Evaluation: estimation of treatment potential toxicity using BED-based dose conversion and Normal Tissue Complication Probability (NTCP) modeling.

Table 4.1: BED constraints for different organs.

Organs	**BED constraints**
Chest wall ($\alpha/\beta = 3Gy$)	**D70cc < 38.3 Gy** **D2cc < 216.7 Gy**
Ribs ($\alpha/\beta = 3Gy$)	**D2cc < 109.3 Gy**
Lungs-ITV ($\alpha/\beta = 3Gy$)	**V53.5Gy < 10%** **D1500cc < 22.8 Gy** **D1000cc < 25.1 Gy**

By integrating these three evaluation methodologies, a comprehensive assessment of the treatment plans is conducted, allowing for an objective comparison of IMPT, CIRT, and VMAT. The following sections provide a detailed explanation of each evaluation method and the parameters used for comparison. Moreover, a statistical analysis was performed to evaluate differences in the numerical parameters among the various radiation modalities. Given the nature of the data, comparisons were conducted using the Wilcoxon signed-rank test, a non-parametric method suitable for paired data that do not necessarily follow a normal distribution. A p-value threshold of 0.05 was adopted to determine statistical significance, ensuring that any observed differences were unlikely to have occurred by chance. All statistical evaluations were carried out using Python (Version 3.11.1).

4.1 Dosimetric evaluation

The dosimetric evaluation aims to assess the ability of each treatment modality to deliver an optimal dose distribution to the CTV while minimizing exposure to OARs. This analysis is fundamental to ensuring that the prescribed dose is adequately delivered to the target, achieving sufficient tumor control while reducing the probability of normal tissue complications. To make this comparison, several dosimetric parameters were analyzed in the following sections.

A. Isodose distribution charts

Isodose distribution charts provide a visual representation of the dose distribution within an irradiated volume. They display lines, known as isodose curves, which connect all points receiving the same dose value. These curves provide a quick visualization of how well the dose is concentrated within the target and how it spreads to the surrounding healthy tissues. This allows for a rapid assessment of whether a treatment plan is well optimized.

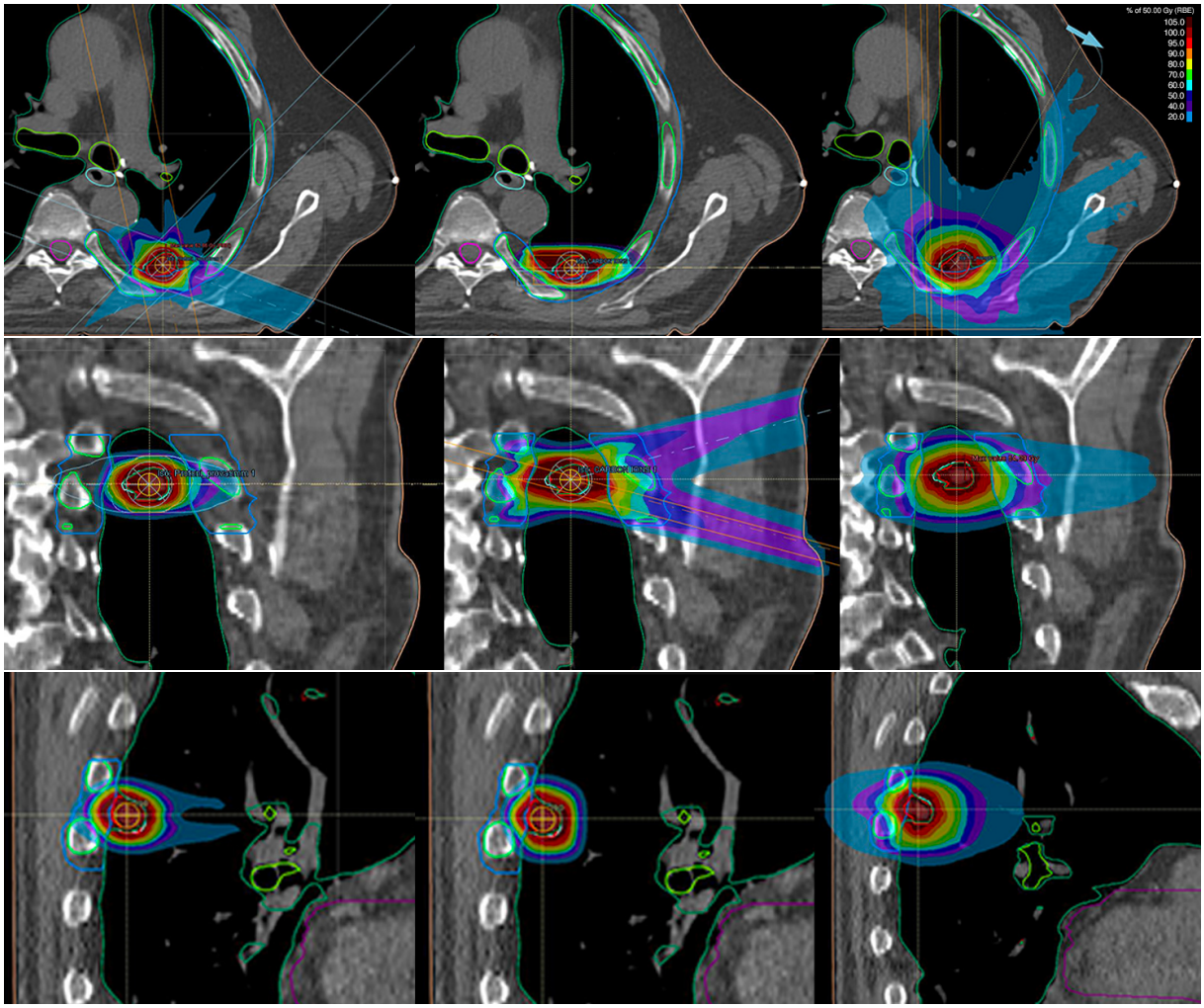

Figure 4.1: RBE-weighted dose distribution comparison across IMPT (left), CIRT (center), and VMAT (right) in axial (top), coronal (middle), and sagittal (bottom) views, generated from the RayStation TPS. In addition to the CTV, the images also display the delineation of OARs, highlighting the chest wall (outlined in blue) and ribs (outlined in neon green).

Figure 4.1 presents the RBE-weighted dose distributions for the three treatment techniques under investigation. Specifically, it compares the isodose distributions over CT

images in the axial, coronal, and sagittal planes, ranging from 20% to 105% of the prescription dose. The images highlight key differences among the treatment techniques. In particular, IMPT and CIRT demonstrate greater dose conformity compared to VMAT, thereby reducing irradiation to surrounding healthy tissues. Additionally, the transition between high- and low-dose regions appears sharper in particle-based techniques (IMPT and CIRT) compared to VMAT, which exhibits a more gradual dose gradient. Consequently, a preliminary analysis of the isodose charts suggests that IMPT and CIRT provide better protection of OARs due to their more focused dose distribution compared to VMAT.

B. Dose-volume histograms (DVHs)

DVHs, used to quantify dose distribution across the CTV and OARs, are graphical representations employed to analyze dose distribution in treatment plans. Cumulative DVH illustrate the fraction of the volume of an organ receiving at least a given dose. In general, a steeper DVH with a shape closer to a rectangle indicates better dose homogeneity within the target, whereas for OARs, an ideal DVH presents a rapid decline, indicating that a smaller volume of the organ receives high doses, thereby ensuring effective dose sparing in healthy tissues.

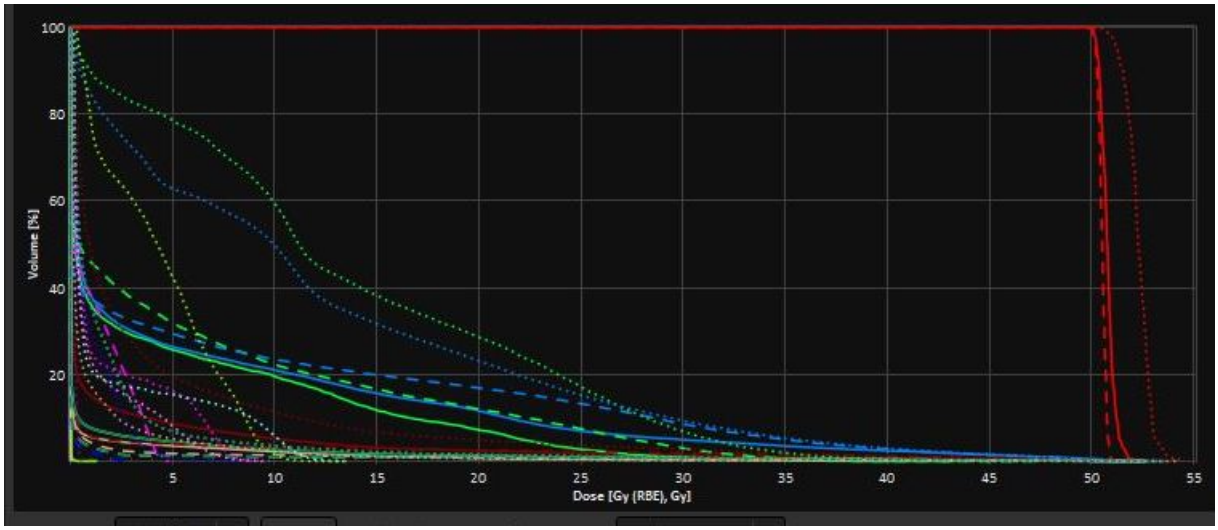

Figure 4.2: Cumulative DVHs comparing the three treatment techniques: IMPT (solid lines), CIRT (dashed lines), and VMAT (dotted lines). The red curve represents the CTV, while the other colored curves correspond to different OARs. The graph illustrates the differences in dose distribution among the techniques, highlighting the sparing of OARs achieved with IMPT and CIRT compared to VMAT.

C. Dosimetric indices

Dosimetric indices, such as the HI, CI, and GI, provide quantitative measures of how well the dose conforms to the target and spares surrounding tissues. A more detailed discussion

of these indices has been provided in 3.2. To clinically interpret the results, it is essential

Table 4.2: Comparison of dosimetric indices (mean (SD)) across IMPT, CIRT, and VMAT.

Measure	**IMPT**	**CIRT**	**VMAT**	p^a	p^b	p^c
HI	0.05 (0.02)	0.03 (0.01)	0.06 (0.01)	<0.001	0.063	<0.001
CI	0.51 (0.15)	0.51 (0.15)	0.63 (0.09)	0.155	0.013	0.013
GI	8.64 (4.13)	8.64 (4.13)	19.25 (11.35)	0.888	<0.001	<0.001

[a] p-value for the comparison between IMPT and CIRT.
[b] p-value for the comparison between IMPT and VMAT.
[c] p-value for the comparison between CIRT and VMAT.

to consider both the ideal values of the dosimetric indices and their statistical significance (presented in Table 4.2). Regarding the HI, whose ideal value is $HI = 0$, IMPT resulted in a 16.7% reduction compared to VMAT (p = 0.063), suggesting that the difference between the two techniques is not statistically significant. In contrast, CIRT achieved a 50% reduction (p < 0.001), indicating a highly significant difference. For the CI, whose ideal value is 1, both IMPT and CIRT led to a 19% reduction compared to VMAT (p = 0.013), demonstrating a lower conformity relative to photon-based treatment. Both IMPT and CIRT proved highly effective in reducing the GI, showing a 55.1% reduction compared to VMAT. Specifically, the difference between CIRT and VMAT was highly significant (p < 0.001), whereas the difference between IMPT and VMAT (p = 0.888) was not statistically significant. Regarding the statistical analysis in this study, it should be noted that the small cohort of 20 patients may limit the ability to detect statistically significant differences between the investigated techniques, potentially affecting the robustness of the findings.

D. CTV coverage, high-dose regions and OAR constraints

CTV coverage and high-dose regions were assessed through D5%, which represents the dose received by the most irradiated 5% of the target volume and serves as a crucial indicator of dose homogeneity, along with OAR constraints expressed in BED, ensuring a biologically relevant comparison across different fractionation schemes. As reported in Table 4.3, target coverage meets clinical objectives (V100% $\geq$ 95%) for all three compared techniques, with minimal differences that are not statistically significant. Regarding the maximum dose within the target, assessed using D5% < 107% (i.e., the dose absorbed by the most irradiated 5% of the CTV volume), this threshold is met by all three techniques. However, CIRT achieves a slightly lower D5%, with a statistically significant difference (p < 0.001) compared to both IMPT and VMAT. For OARs, IMPT and CIRT consistently show lower dosimetric values compared to VMAT, except for V53.5Gy in Lung-ITV, where CIRT records the highest value. Specifically, in the chest wall, D70cc and D2cc were reduced by 89.3% and 22.6% with IMPT (p < 0.001) and by 80.0% and 6.7% with

Table 4.3: RBE-weighted dosimetric parameters (mean (SD)) for targets and OARs across IMPT, CIRT, and VMAT plans. CTV results are expressed as percentages (%), while OAR values are reported as doses in Gy (BED).

Region	**Measure**	**IMPT**	**CIRT**	**VMAT**	p^a	p^b	p^c
CTV	V100%	99.27 (0.77)	99.24 (0.69)	98.59 (1.63)	0.386	0.062	0.062
	D5%	105.27 (2.29)	103.56 (1.62)	105.98 (0.96)	<0.001	0.360	<0.001
Chest Wall	D70cc	1.72 (5.51)	3.22 (8.53)	16.10 (9.66)	0.418	<0.001	<0.001
	D2cc	120.33 (54.21)	144.99 (43.88)	155.41 (47.82)	0.001	<0.001	0.105
Ribs	D2cc	68.86 (33.59)	83.69 (25.15)	111.38 (36.02)	0.004	<0.001	<0.001
Lungs-ITV	V53.5Gy	2.08 (1.25)	3.09 (1.75)	2.96 (1.49)	0.059	0.023	0.898
	D1500cc	0.12 (0.46)	0.01 (0.38)	1.38 (1.59)	0.003	<0.001	<0.001
	D1000cc	0.63 (2.54)	0.07 (0.23)	2.94 (3.14)	0.048	<0.001	<0.001

[a] p-value for the comparison between IMPT and CIRT.
[b] p-value for the comparison between IMPT and VMAT.
[c] p-value for the comparison between CIRT and VMAT.

CIRT ($p < 0.001$ and $p = 0.105$, respectively). In the ribs, D2cc was reduced by 38.2% with IMPT ($p < 0.001$) and by 24.9% with CIRT ($p < 0.001$). Regarding Lungs-ITV, V53.3Gy decreased by 29.7% with IMPT ($p = 0.023$), whereas it increased by 4.4% with CIRT ($p = 0.898$). Additionally, D1500cc was reduced by 91.3% with IMPT ($p < 0.001$) and by 99.3% with CIRT ($p < 0.001$), while D1000cc was reduced by 78.6% with IMPT ($p < 0.001$) and by 97.6% with CIRT ($p < 0.001$). Statistically significant differences between IMPT and CIRT were observed for D5% of the CTV ($p < 0.001$), D2cc of the Chest Wall ($p = 0.001$), D2cc of the Ribs ($p = 0.004$), and D1500cc of Lungs-ITV ($p = 0.003$).

4.2 Robust evaluation

In radiation therapy, treatment plan robustness refers to the ability to maintain adequate target coverage and OAR sparing despite uncertainties in patient positioning and tissue heterogeneity. This aspect is particularly critical for particle therapy techniques, such as IMPT and CIRT, where range uncertainties pose a significant challenge. Unlike photon-based VMAT, where dose deposition can also be affected by setup uncertainties and variations in tissue composition but remains relatively stable, proton and carbon ion beams exhibit a well-defined Bragg peak, making their range highly susceptible to even small errors, which can significantly impact treatment accuracy. Beyond the physical characteristics of the particles used, robust evaluation is also crucial for the type of lesions under consideration. As previously discussed (see section 2.6), lung lesions are particularly subject to respiratory motion, making it essential to ensure that the dose

distribution remains robust to positioning uncertainties, tissue density variations, and target motion, which can further impact treatment accuracy. Due to the inherent differences in physical dose deposition and sensitivity to uncertainties, a structured robustness analysis was conducted to assess the reliability of each treatment modality under realistic clinical conditions. Patient positioning uncertainty, defined as the maximum displacement relative to the isocenter, was set to 3 mm along the antero-posterior, left-right, and superior-inferior directions, in agreement with previous studies ([40, 41]). Similarly, density uncertainty was set to 3.5% following values reported in the literature [42]. Figure 2.7 shows the RayStation interface where these parameters were set to generate the 18 dose scenarios required for robustness evaluation.

In clinical practice, a commonly used method for visualizing and reporting robustness includes DVH curves, which illustrate an example of the dose distribution across the various simulated scenarios. Figure 4.3 presents DVHs for the CTV across different robustness analysis scenarios, comparing IMPT (top), CIRT (middle), and VMAT (bottom). Focusing on CTV coverage, it can be observed that for all three techniques, the CTV receives the full prescription dose (in this case, 50 Gy), with a sharp dose fall-off beyond this value, ensuring good target coverage and minimal dose spill into surrounding tissues. However, differences in robustness can be observed among the modalities. IMPT and CIRT exhibit slightly greater variability in DVHs across robustness scenarios, suggesting a higher sensitivity to uncertainties. In contrast, VMAT demonstrates lower variability across different robustness scenarios.

Similarly, Figure 4.4 presents DVHs for the OARs across different robustness analysis scenarios, comparing IMPT (top), CIRT (middle), and VMAT (bottom). Across all three techniques, the dose to the chest wall and ribs gradually decreases with increasing volume, meaning that only a small portion of these structures receives a high dose. The maximum dose values for both structures are highest in the VMAT plan, suggesting a broader dose distribution compared to IMPT and CIRT. Regarding robustness scenarios, IMPT and CIRT exhibit relatively narrow bands of variability, indicating that changes in setup or range uncertainties have a minimal impact on the dose distribution to the OARs. In contrast, VMAT shows greater variability in the DVHs, particularly at lower dose levels, suggesting that the dose to OARs is more susceptible to changes in the treatment scenario.

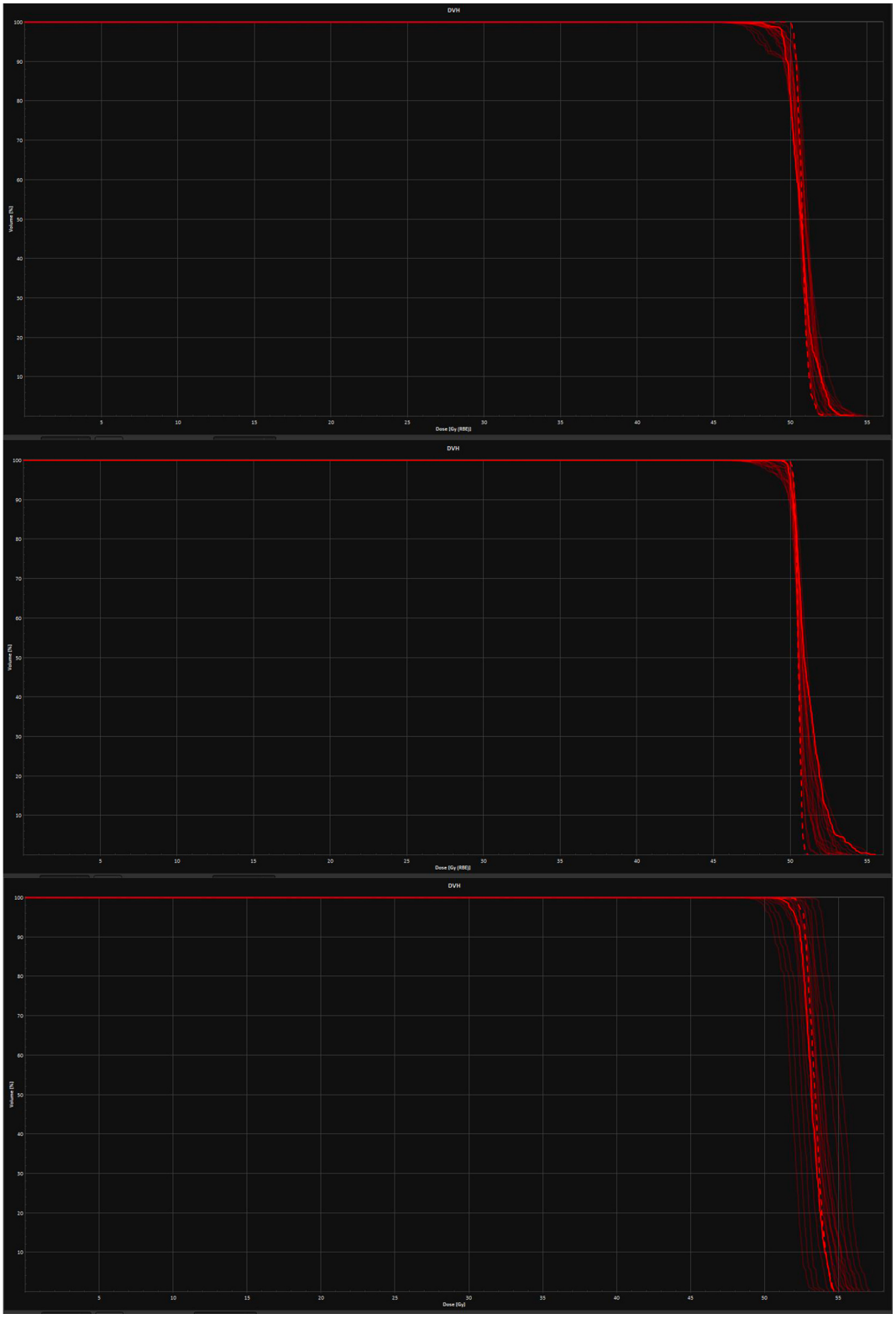

Figure 4.3: DVHs for the CTV across different robustness analysis scenarios. The solid red line represents the reference scenario, while the DVHs for all other robustness scenarios are displayed in transparency. The top figure corresponds to IMPT, the middle to CIRT, and the bottom to VMAT.

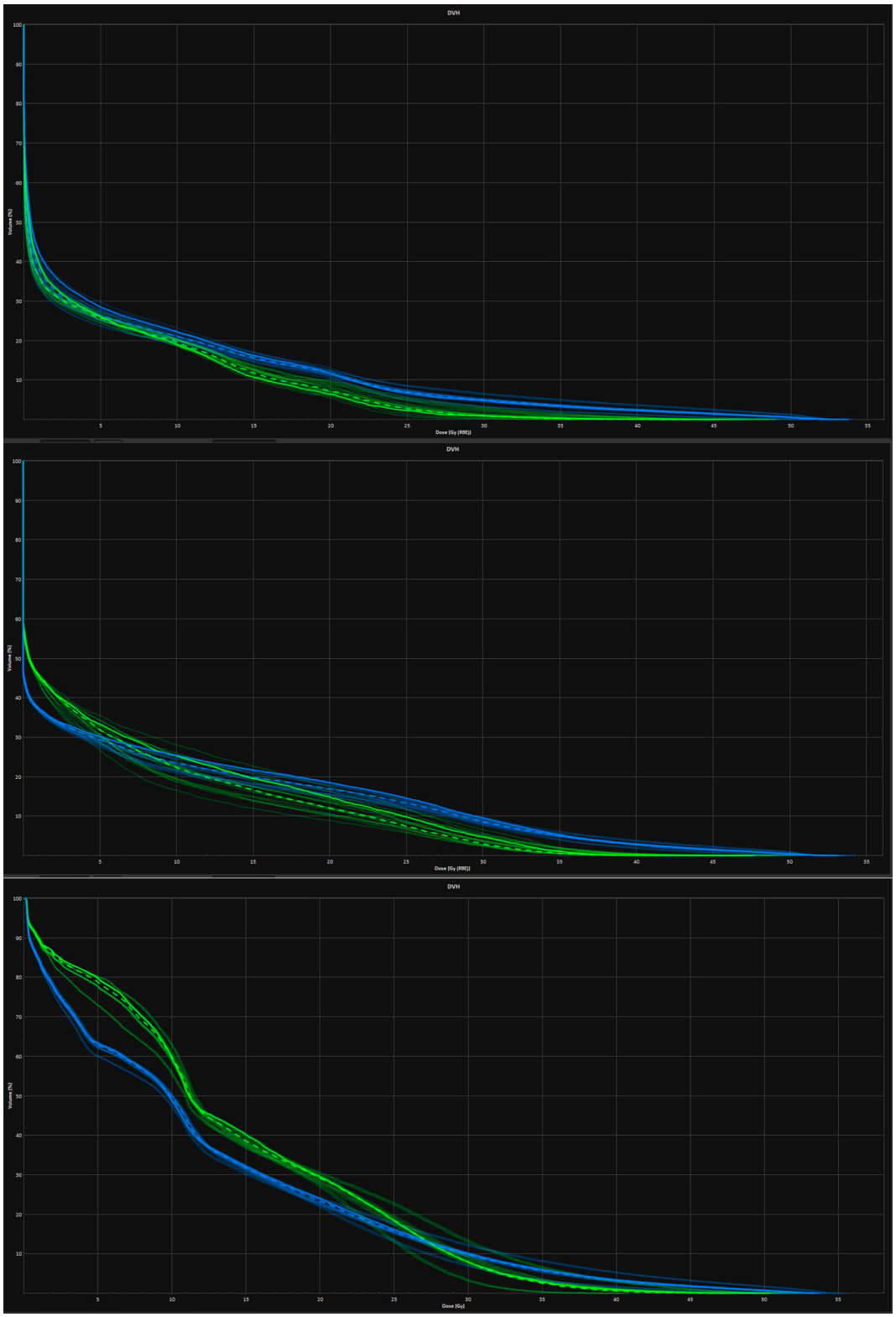

Figure 4.4: DVHs for the OARs across different robustness analysis scenarios. The blue lines correspond to the chest wall, while the green lines represent the ribs. The top figure corresponds to IMPT, the middle to CIRT, and the bottom to VMAT.

While DVHs provide valuable insights for robustness analysis and serve as an essential evaluation tool, they primarily offer a qualitative representation of dose distribution. To achieve a more precise and quantitative assessment, the worst-case scenario approach, a widely adopted method in clinical studies, was employed to evaluate OARs dose and target coverage. The robustness evaluation aimed to assess the impact of patient positioning and density uncertainties on target coverage, dose homogeneity, and OARs sparing. Each plan was analyzed based on the percentage of simulated scenarios that met the predefined clinical criteria. For each treatment modality, the percentage of scenarios satisfying the clinical objectives was quantified (Table 4.4). In cases where the clinical criteria for OARs (see Table 4.1) were not met, a worst-case analysis was performed to evaluate the extent of deviation and its potential clinical impact (Table 4.5). Regarding the robustness analysis for the CTV, a stringent planning objective of $V100\% \geq 95\%$ was initially set for the dosimetric evaluation. However, for robustness evaluation, a different metric was adopted: $D95\% > 95\%$. This parameter, slightly less restrictive, provides a more practical assessment of target coverage under uncertainty conditions. The choice of D95% as a robustness evaluation metric is widely recognized in clinical practice and is consistent with the recommendations of ICRU Report 83 [43]. Similarly, for dose homogeneity assessment, the robustness evaluation considers $D5\% < 107\%$, a parameter that allows for a more realistic evaluation of potential dose variations across different scenarios, particularly in intensity-modulated treatments, while remaining aligned with the same guidelines.

Table 4.4: Percentage of satisfied scenarios (mean(SD)) for CTV coverage, CTV high-dose regions, and OAR constraints across IMPT, CIRT, and VMAT plans.

	CTV		**OAR**	
	D95%	D5%	Chest wall D2cc	Ribs D2cc
IMPT	18.6% (16.1)	59.8% (35.2)	94.5% (19.3)	90.6% (25.0)
CIRT	23.9% (16.2)	78.3% (29.8)	91.7% (18.1)	83.9% (26.8)
VMAT	74.0% (14.1)	58.6% (33.1)	88.2% (15.6)	53.1% (42.7)

Examining the percentage of scenarios in which 95% of the CTV receives the prescribed dose, the results presented in Table 4.4 indicate that VMAT provides the most stable target coverage, with a significantly higher proportion of satisfied scenarios compared to IMPT and CIRT. Regarding the percentage of scenarios in which the most irradiated 5% of the CTV remains below the maximum dose threshold, CIRT demonstrates superior control over the maximum dose within the target, as indicated by the highest percentage of satisfied scenarios. IMPT and VMAT yield similar percentages, with a slightly higher value for IMPT. This finding is consistent with the fact that VMAT lacks the characteristic Bragg peak of charged particles, leading to a more diffuse dose distribution and an increased risk of overdose in certain areas. Analyzing the dose constraints for OARs, IMPT and CIRT provide more robust protection compared to VMAT in terms of the percentage of scenarios where the maximum dose to 2cc of the chest wall is within the

Table 4.5: Average doses in the worst-case scenario for cases that do not meet robustness criteria in CTV coverage, CTV high-dose regions, and OAR constraints across IMPT, CIRT, and VMAT plans.

	CTV		**OAR***	
	D95%	D5%	Chest wall D2cc	Ribs D2cc
IMPT	93.5%	111.5%	247.58	147.71
CIRT	93.6%	110.4%	231.35	131.22
VMAT	98.4%	110.3%	220.27	147.70

* The values in the OAR column are doses expressed in Gy(BED).

prescribed limit. Specifically, both IMPT and CIRT satisfy the constraint in over 90% of scenarios (94.5% and 91.7%, respectively). The superior robustness of IMPT and CIRT compared to VMAT in OAR protection is further confirmed by the percentage of scenarios satisfying the dose constraint to 2cc of the ribs. IMPT and CIRT guarantee a much more stable protection of the ribs with 90.6% and 83.9% of satisfied scenarios respectively, while VMAT satisfies the constraint only in 53.1% of cases, indicating a poor robustness. In the worst-case scenario analysis presented in Table 4.5, all three techniques show variations in target coverage. Specifically, VMAT appears to be the most robust technique in terms of maintaining the prescribed dose, with D95% = 98.4%, exceeding the 95% threshold. Conversely, both IMPT and CIRT fall slightly below this limit, with D95% values of 93.5% and 93.6%, respectively. Regarding high-dose regions,all three techniques exceed the dose limit (D5%<107%), highlighting the challenge of effectively controlling high-dose regions across all modalities. Although in the worst cases the dose may exceed the constraints in all three techniques, IMPT and CIRT are more robust than VMAT in protecting OARs, ensuring a greater number of scenarios in which the constraints are respected. In clinical practice, IMPT and CIRT could be advantageous by offering less variability in the dose to OARs with a lower risk of toxicity compared to VMAT. For this purpose, radiobiological analysis is essential to assess the biological implications of dose variations across different techniques, thereby guiding treatment optimization and clinical decision-making.

4.3 Radiobiological evaluation

The evaluation of treatment plans should not be limited to dosimetric parameters alone, as they do not fully capture the biological effects of radiation on healthy tissues. To complement the dosimetric analysis, a radiobiological assessment was performed by estimating the NTCP for IMPT, CIRT, and VMAT, using the Lyman-Kutcher-Burman (LKB) model [44]. The model describes the relationship between the received dose and the probability of developing adverse effects through a sigmoidal curve. The shape of this curve is determined by empirical parameters derived from retrospective studies. The

classical expression of the LKB model is as follows:

$$\text{NTCP} = \frac{1}{\sqrt{2\pi}} \int_{-\infty}^{t} e^{-\frac{x^2}{2}}\, dx \tag{4.1}$$

where the value of t is defined as:

$$t = \frac{D_{opt} - TD_{50}}{m \times TD_{50}} \tag{4.2}$$

In this formulation: D_{opt} represents the effective dose received by the tissue, traditionally expressed as the Equivalent Uniform Dose (EUD); TD_{50} denotes the dose at which 50% of patients develop the considered complication; and m is an empirical parameter that governs the slope of the sigmoidal curve, determining the rate at which the complication probability increases with dose escalation. The EUD is a concept introduced to represent a non-uniform dose distribution with a single equivalent value that produces the same biological effect. The EUD is defined by the following equation:

$$EUD = \left(\sum_{i=1}^{N} v_i \times D_i^{\frac{1}{n}} \right)^n \tag{4.3}$$

where D_i is the dose received by each subvolume v_i in the DVH; v_i represents the volume corresponding to each dose bin; N is the total number of subvolumes considered; and n is a parameter that characterizes the organ's response based on its structural properties. As previously discussed in Section 2.2.1, serial organs are highly sensitive to damage in small subvolumes, necessitating low n values. In contrast, parallel organs exhibit greater tolerance to focal damage, resulting in higher n values.
In the present study, the LKB model was adapted using doses expressed in BED instead of EUD or EQD2 (see Eq.(1.30)). The BED accounts for both the total dose and the fractionation scheme, providing a more accurate representation of the biological effect of radiation on a specific tissue. To ensure consistency, both the dose derived from the DVH and the TD_{50} value were converted into the BED domain, thereby eliminating the need for intermediate conversions such as EQD2.
The NTCP model provides a quantitative estimate of the likelihood of developing radiation-induced toxicities based on the dose distribution in critical structures. In this study, two clinically relevant toxicities were analyzed:

- Radiation-induced pneumonitis (RP);
- Rib fractures (RF) due to radiation-induced bone damage.

For each treatment modality, NTCP calculations were performed using DVHs extracted from the treatment plans, allowing for a direct comparison. The estimation was based on literature-derived parameters specific to lung toxicity and bone complications.

4.3.1 Radiation-induced pneumonitis

Radiation-induced pneumonitis (RP) is one of the most common and clinically significant complications of thoracic radiotherapy. In SBRT, the high dose conformality allows for

reduced irradiation of the healthy lung; however, the aggressive hypofractionation employed may influence the risk of toxicity. To assess the risk of toxicity for this endpoint, NTCP was calculated for both the ipsilateral lung and the ipsilateral lung excluding the ITV. In both cases, mean lung dose (MLD) was used as a predictive factor for radiation-induced lung toxicity, as it is a well-established dosimetric predictor, particularly in the context of 3D-CRT [45]. However, data on the correlation between MLD and NTCP in SBRT remain more limited. The choice of NTCP calculation for the ipsilateral lung was justified by the fact that SBRT delivers highly conformal radiation, resulting in minimal involvement of the contralateral lung. Supporting this approach, studies such as Willner et al. [46] have reported that separate lung analysis yields more reliable NTCP predictions compared to whole-lung considerations. Meanwhile, the choice of NTCP calculation for the ipsilateral lung excluding the ITV was based on the rationale that this approach excludes the tumor volume, focusing solely on the radiation exposure to the surrounding healthy lung tissue. In accordance with Ricardi et al. [47], the following parameters were used to calculate NTCP: TD_{50} = 24.5 Gy, and m = 0.18.

Table 4.6: NTCP values (mean (SD)) for Lung Ipsilateral and Lungs-ITV across IMPT, CIRT, and VMAT plans. Min and Max values are reported in brackets below each mean value. All NTCP values are expressed as percentages (%).

Region	**IMPT**	**CIRT**	**VMAT**	p^a	p^b	p^c
Lung Ipsilateral	0.43 (0.09)	0.42 (0.03)	0.59 (0.21)	0.257	0.004	<0.001
	[0.39 - 0.80]	[0.39 - 0.48]	[0.39 - 1.14]			
Lungs-ITV	0.41 (0.05)	0.40 (0.01)	0.43 (0.09)	0.317	0.058	0.058
	[0.39 - 0.60]	[0.39 - 0.43]	[0.39 - 0.80]			

[a] p-value for the comparison between IMPT and CIRT.
[b] p-value for the comparison between IMPT and VMAT.
[c] p-value for the comparison between CIRT and VMAT.

The mean NTCP for radiation-induced pneumonitis, calculated based on the mean dose to the ipsilateral lung, was 0.43% for IMPT, 0.42% for CIRT, and 0.59% for VMAT. The absolute differences between the techniques are very small (<0.05%), indicating that the risk of this complication is clinically similar across the three approaches. Moreover, the reductions observed with IMPT and CIRT compared to VMAT, although modest, were statistically significant, with p = 0.004 for the comparison between IMPT and VMAT and p < 0.001 for CIRT and VMAT. Regarding the mean NTCP calculated based on Lungs-ITV, values were 0.41% for IMPT, 0.40% for CIRT, and 0.43% for VMAT. However, in this case, the differences between the particles and the photon techniques were not statistically significant (p = 0.058). Finally, when comparing the two particle therapy techniques, no statistically significant differences were found in NTCP, either for the mean dose to the ipsilateral lung or for Lungs-ITV (p = 0.257 and p = 0.317, respectively).

4.3.2 Rib fractures

Rib fractures may occur due to high-dose exposure, particularly in particle therapy, where the dose distribution tends to be more localized but also more intense in specific regions. Rib fractures following SBRT are generally more frequent compared to other radiotherapy techniques; however, their reported incidence varies depending on the method of assessment—whether based on clinically relevant (symptomatic) fractures or asymptomatic fractures detected on follow-up CT scans. In accordance with Stam et al. [48], this study employed D_2cc as the predictive dosimetric parameter for NTCP calculations on both the ribs and the chest wall, despite D_{max} often being identified as the dominant prognostic factor for rib fractures. This choice is particularly relevant given that Dmax is highly sensitive to setup errors, tumor motion, and range uncertainties in particle therapy, factors that are especially significant in this study, which compares IMPT, CIRT, and VMAT. Consequently, D_2cc is a more robust predictor, as it is less susceptible to variations due to setup errors and more stable against respiratory motion, particularly in proton and carbon ion therapy plans. Furthermore, the decision to evaluate NTCP for both the ribs and the chest wall is supported by the need to avoid underestimating the overall treatment toxicity. Restricting the analysis solely to the ribs could overlook relevant toxic effects in adjacent structures. Additionally, this dual analysis enhances comparability across IMPT, CIRT, and VMAT, as each technique distributes dose differently between the ribs and the chest wall. From [48] the following parameters were used to calculate NTCP:TD_{50} = 452Gy, and m = 0.329.

Table 4.7: NTCP values (mean (SD)) for Chest Wall and Ribs across IMPT, CIRT, and VMAT plans. Min and Max values are reported in brackets below each mean value. All NTCP values are expressed as percentages (%).

Region	**IMPT**	**CIRT**	**VMAT**	p^a	p^b	p^c
Chest Wall	7.35 (1.50) [5.37 - 10.58]	8.00 (1.30) [5.98 - 10.36]	8.33 (1.34) [5.41 - 9.84]	0.005	<0.001	0.090
Ribs	5.99 (0.85) [4.97 - 8.98]	6.32 (0.59) [5.31 - 7.18]	7.03 (0.92) [5.29 - 8.81]	0.007	<0.001	<0.001

[a] p-value for the comparison between IMPT and CIRT.
[b] p-value for the comparison between IMPT and VMAT.
[c] p-value for the comparison between CIRT and VMAT.

The mean NTCP for rib fractures, evaluated using D2cc to the chest wall, was 7.35% for IMPT, 8.00% for CIRT, and 8.33% for VMAT. IMPT showed an absolute reduction of 0.98% compared to VMAT ($p < 0.001$), while CIRT showed an absolute reduction of 0.33% compared to VMAT, although this difference was not statistically significant ($p = 0.09$). Regarding the mean NTCP for rib fractures, evaluated using D2cc to the ribs, values were 5.99% for IMPT, 6.32% for CIRT, and 7.03% for VMAT. IMPT showed an absolute reduction of 1.04% compared to VMAT ($p < 0.001$), while CIRT showed an absolute

reduction of 0.71% compared to VMAT ($p < 0.001$). These results indicate that IMPT and CIRT reduce the risk of rib fractures compared to VMAT, with IMPT demonstrating the most pronounced reduction. Moreover, these differences are statistically highly significant. Finally, when comparing IMPT and CIRT, no statistically significant differences were found.

Chapter 5

Conclusions

In this thesis, the advantages of IMPT, using collimated beams, and CIRT were highlighted through a comparison with VMAT. All three techniques were evaluated within the context of SBRT for lung cancer. The dosimetric analysis showed the most significant advantages, particularly in terms of OAR sparing, aimed at minimizing radiation-induced toxicity. The results of this analysis revealed statistically significant differences in favor of particle therapy, aligning with theoretical expectations, which highlight the Bragg peak as a key feature that enables a highly localized dose deposition within the tumor, reducing irradiation to healthy tissues. The robust analysis, conducted to account for potential uncertainties due to range errors, setup errors, and organ motion caused by respiration, was crucial for this type of study. Charged particles, such as protons and carbon ions, are particularly sensitive to variations in range, and the treated lesions are highly responsive to respiratory motion. The robustness analysis demonstrated that VMAT provides the most stable target coverage, while CIRT offers better control over overdose regions. Furthermore, concerning OAR sparing, particularly for the chest wall and ribs, both IMPT and CIRT proved more effective. The advantage of CIRT over IMPT in the robustness evaluation can be attributed to the higher mass of carbon ions, which results in reduced sensitivity to range uncertainties, leading to greater stability and fewer fluctuations in dose delivery to organs at risk. Finally, the radiobiological analysis allowed for the evaluation of NTCP for radiation-induced pneumonitis and rib fractures. Regarding radiation-induced pneumonitis, the NTCP values obtained indicated a very low risk for all studied techniques. However, although NTCP differences were modest in absolute terms, a statistically significant advantage was observed for IMPT and CIRT over VMAT. Regarding rib fractures, for both evaluated metrics, IMPT and CIRT showed a reduction in NTCP compared to VMAT. Additionally, IMPT exhibited the greatest reduction, supported by statistical significance across all metrics.
To provide a comprehensive evaluation, it is necessary to highlight the critical aspects of this study, suggesting potential improvements for future developments. One major limitation in CIRT treatment planning is the lack of widely established and clinically applicable protocols for lung tumors treated with carbon ions. To ensure consistency in comparisons, CIRT plans were created using the same fractionation schemes and pre-

scriptions as IMPT and VMAT. Although this choice may not fully reflect the clinical potential of CIRT in the SBRT context, the NTCP evaluation remains valid, as it allows for the assessment of the biological impact of the three techniques on healthy tissues independent of specific protocols. Interpreting the NTCP results within the methodological framework chosen, it is likely that an optimized protocol for CIRT could further enhance the benefits of this treatment approach. Another critical factor concerns the use of the LEM I and uncertainties in the evaluation of the RBE. Although LEM I is a validated model for carbon ion radiotherapy, it has limitations when applied to hypofractionated regimens, such as those used in SBRT. Additionally, an important consideration is that NTCP models were originally developed for photon-based radiotherapy and later adapted for particle therapy. However, these adaptations introduce limitations due to the physical differences in interactions between charged particles and photons. The development of NTCP models specifically for charged particles, based on real-world clinical registry data, will be essential for optimizing treatments and improving treatment planning quality in particle therapy. Finally, regarding the cohort of patients analyzed in this in silico study, two aspects must be emphasized.

- First, the limited sample size: with only 20 patients, the statistical analysis loses reliability, reducing its statistical power.
- Second, all patients included in the study had peripheral lung tumors, reducing the variability of the sample and limiting the generalizability of the findings.

This study has demonstrated the possible advantages of IMPT and CIRT over VMAT in SBRT for lung cancer with regards to OAR sparing and reduced NTCP for rib fractures and radiation pneumonitis. Although some methodological uncertainties coupled and the limited sample size reduce the generalizability of the findings, the results further support the use of particle therapy in this context. Future studies should aim to validate these findings in larger cohorts, including centrally located lung tumors and optimizing CIRT specific protocols. Moreover, proton and carbon ion therapy NTCP models based on real-world clinical data will need to be developed for accurate toxicity prediction and treatment planning. The implementation of these strategies could lead to an increasingly personalized approach to therapy, maximizing oncological efficacy while minimizing side effects, with a significant impact on the quality of life of patients undergoing SBRT for lung cancer.

Bibliography

[1] G. Knoll, John Wiley, 2010, ISBN 978-0-470-13148-0

[2] F. Salvat and J. M. Fernández-Varea, "Overview of physical interaction models for photon and electron transport used in Monte Carlo codes," *Metrologia*, vol. 46, no. 2, pp. S112, 2009. DOI: 10.1088/0026-1394/46/2/S08.

[3] E. B. Podgorsak, *Radiation Physics for Medical Physicists*, 3rd ed., With 232 Figures, 98 Tables. Springer, 2016.

[4] K. Cengel, E. S. Diffenderfer, S. Avery, J. McDonough, "Using electron beam radiation to simulate the dose distribution for whole body solar particle event proton exposure," *Radiation and Environmental Biophysics*, vol. 49, no. 4, pp. 715-721, Nov. 2010. doi: 10.1007/s00411-010-0315-z.

[5] D. Schardt, T. Elsässer, and D. Schulz-Ertner, *Heavy-ion tumor therapy: Physical and radiobiological benefits*, Rev. Mod. Phys., vol. 82, no. 1, pp. 383–425, Feb. 2010. doi: 10.1103/RevModPhys.82.383.

[6] H. E. S. Pettersen, "A Digital Tracking Calorimeter for Proton Computed Tomography," PhD thesis, May 2018. Advisors: D. Röhrich, O. H. Odland, I. Meric.

[7] Haijo Jung, "Basic Physical Principles and Clinical Applications of Computed Tomography," *Progress in Medical Physics*, vol. 32, no. 1, pp. 1–17, March 2021. DOI: 10.14316/pmp.2021.32.1.1.

[8] G. Magro, *CERN Academic Training on Hadron Therapy - Robust Treatment Planning and Plan Verification Strategies in Scanning Ion Beam Therapy (2/5)*, CERN Academic Training Regular Programme, 31 October 2023. Available at: `https://indico.cern.ch/event/1335920/`.

[9] S. J. McMahon and K. M. Prise, *Mechanistic Modelling of Radiation Responses*, Centre for Cancer Research & Cell Biology, Queen's University Belfast, Northern Ireland, UK, Received: 20 November 2018; Accepted: 6 February 2019; Published: 10 February 2019.

[10] Japan Atomic Energy Agency, "Development of Advanced Radiotherapy Using Charged Particle Beams," *RD Review*, vol. 6, no. 5, 2007. Available at: `https://rdreview.jaea.go.jp/review_en/2007/e2007_6_5.html`.

[11] E. J. Hall and S. Willson, *Radiobiology for the Radiologist*, 8th ed., Wolters Kluwer, 2023.

[12] S. J. McMahon, "The linear quadratic model: usage, interpretation and challenges," *Phys. Med. Biol.*, vol. 64, 01TR01, 2019. DOI: 10.1088/1361-6560/aaf26a.

[13] J. Valentin, *Relative biological effectiveness (RBE), quality factor (Q), and radiation weighting factor (wR): ICRP Publication 92: Approved by the Commission in January 2003*, Annals of the ICRP, vol. 33, no. 4, pp. 1-121, 2003. doi: 10.1016/S0146-6453(03)00024-1.

[14] H. Paganetti, *Relative biological effectiveness (RBE) values for proton beam therapy: Variations as a function of biological endpoint, dose, and linear energy transfer*, Physics in Medicine Biology, vol. 59, no. 22, pp. R419–R472, 2014, Institute of Physics and Engineering in Medicine.

[15] J. Loeffler and M. Durante, *Charged particle therapy—optimization, challenges and future directions*, Nat. Rev. Clin. Oncol., vol. 10, no. 7, pp. 411–424, 2013, https://doi.org/10.1038/nrclinonc.2013.79.

[16] Friedrich, Thomas, Durante, Marco, Scholz, Michael. "The Local Effect Model – Principles and Applications." GSI Helmholtzzentrum fur Schwerionenforschung, Planckstraße 1, 64291 Darmstadt, Germany. Technische Universität Darmstadt, Hochschulstraße 6, 64289 Darmstadt, Germany (2012).

[17] G. Moliere, Z. Naturforsch. A **2** (1947), 133

[18] V. L. Highland, Nucl. Instrum. Meth. **129** (1975), 497 doi:10.1016/0029-554X(75)90743-0

[19] G. R. Lynch and O. I. Dahl, Nucl. Instrum. Meth. B **58** (1991), 6-10 doi:10.1016/0168-583X(91)95671-Y

[20] U. Amaldi and G. Kraft, *Radiotherapy with beams of carbon ions*, Rep. Prog. Phys., vol. 68, pp. 1861–1882, 2005.

[21] K. Prise, *Mechanisms of radiation-induced damage in cells*, Nature Reviews Cancer, vol. 9, pp. 200-210, 2009.

[22] H. Nikjoo, S. Uehara, D. Emfietzoglou, and F.A. Cucinotta, *Track structure in radiation biology: theory and applications*, Radiat. Environ. Biophys., vol. 38, pp. 31–40, 1999.

[23] H. Paganetti, et al., "Relative biological effectiveness (RBE) values for proton beam therapy," *International Journal of Radiation Oncology, Biology, Physics*, vol. 53, no. 2, pp. 407–421, 2002.

[24] International Commission on Radiation Units and Measurements (ICRU), *Prescribing, Recording, and Reporting Photon-Beam Intensity-Modulated Radiation Therapy (IMRT)*, Journal of the ICRU, vol. 10, no. 1, Report 83, Oxford University Press, 2010. DOI: 10.1093/jicru/ndq009.

[25] International Commission on Radiation Units and Measurements (ICRU), *Prescribing, Recording, and Reporting Photon Beam Therapy*, ICRU Report 50, Bethesda, MD, USA, 1993.

[26] T. Landberg, J. Chavaudra, J. Dobbs, et al., *Volumes*, Reports of the International Commission on Radiation Units and Measurements, vol. os-32, no. 1, pp. 3-20, 1999. DOI: 10.1093/jicru_os32.1.3.

[27] M. R. Folkert, R. D. Timmerman, "Stereotactic Ablative Body Radiosurgery (SABR) or Stereotactic Body Radiation Therapy (SBRT)", *Seminars in Radiation Oncology*, vol. 24, no. 3, pp. 147–148, 2014. doi: 10.1016/j.semradonc.2014.02.003

[28] S. M. Meyers, K. Kisling, T. F. Atwood, and X. Ray, *A standardized workflow for respiratory-gated motion management decision-making*, Medical Physics, vol. 48, no. 7, pp. 3456–3468, 2021. doi:10.1002/mp.14921.

[29] B. J. Cooper, Y. Rong, and P. J. Keall, "Motion Management in Stereotactic Body Radiation Therapy," *Journal/Book Name*, Year.

[30] Marcher Thompson and Kenneth E. Rosenzweig. The evolving toxicity profile of SBRT for lung cancer. *Translational Lung Cancer Research*, 7(5):537–546, 2018. doi: 10.21037/tlcr.2018.10.06.

[31] J.-P. J. Voroney, A. Hope, M. R. Dahele, T. Purdy, K. N. Franks, S. Pearson, J. B. C. Cho, A. Sun, D. G. Payne, J.-P. Bissonnette, A. Bezjak, and A. M. Brade, "Chest Wall Pain and Rib Fracture after Stereotactic Radiotherapy for Peripheral Non-small Cell Lung Cancer," *International Journal of Radiation Oncology, Biology, Physics*, vol. 75, no. 3, pp. 787–793, 2009. doi:10.1016/j.ijrobp.2008.12.063.

[32] Hwa Kyung Byun, Min Cheol Han, Kyungmi Yang, Jin Sung Kim, Gyu Sang Yoo, Woong Sub Koom, Yong Bae Kim, *Physical and Biological Characteristics of Particle Therapy for Oncologists*, Cancer Research and Treatment: Official Journal of Korean Cancer Association, Vol. 53, No. 3, pp. 611–620, 2021. DOI: 10.4143/crt.2021.066.

[33] Hyer DE, Bennett LC, Geoghegan TJ, Bues M, Smith BR. *Innovations and the Use of Collimators in the Delivery of Pencil Beam Scanning Proton Therapy.* International Journal of Particle Therapy. 2021. DOI: 10.14338/IJPT-20-00039.1.

[34] K. Yasui, T. Toshito, C. Omachi, K. Hayashi, K. Tanaka, K. Asai, A. Shimomura, R. Muramatsu, and N. Hayashi, "Evaluation of dosimetric advantages of using patient-specific aperture system with intensity-modulated proton therapy for the shallow depth tumor," *J Appl Clin Med Phys*, doi: 10.1002/acm2.12231.

[35] Yaparpalvi R, Garg MK, Shen J, Bodner WR, Mynampati DK, Gafar A, et al. Evaluating which plan quality metrics are appropriate for use in lung SBRT. *Br J Radiol*. 2018;91:20170393. doi:10.1259/bjr.20170393.

[36] International Commission on Radiation Units and Measurements. *ICRU Report 83: Prescribing, Recording, and Reporting Photon-Beam Intensity-Modulated Radiation Therapy (IMRT)*. Journal of the ICRU. 2010;10(1). doi:10.1093/jicru/ndq001.

[37] Paddick I, Lippitz B. *A simple dose gradient measurement tool to complement the conformity index*. Journal of Neurosurgery. 2006;105(Suppl):194-201. doi:10.3171/sup.2006.105.7.194.

[38] Y. Miyasaka, S. Komatsu, T. Abe, N. Kubo, N. Okano, K. Shibuya, K. Shirai, H. Kawamura, J.-i. Saitoh, T. Ebara, et al., "Comparison of Oncologic Outcomes between Carbon Ion Radiotherapy and Stereotactic Body Radiotherapy for Early-Stage Non-Small Cell Lung Cancer," *Cancers*, vol. 13, no. 176, 2021. doi: 10.3390/cancers13020176.

[39] M. Krämer and M. Scholz, "Treatment planning for heavy-ion radiotherapy: calculation and optimization of biologically effective dose," *Physics in Medicine & Biology*, vol. 45, no. 11, pp. 3319, 2000. DOI: 10.1088/0031-9155/45/11/314.

[40] E. Mastella, A. Mirandola, S. Russo, A. Vai, G. Magro, S. Molinelli, A. Barcellini, V. Vitolo, E. Orlandi, and M. Ciocca, "High-dose hypofractionated pencil beam scanning carbon ion radiotherapy for lung tumors: Dosimetric impact of different spot sizes and robustness to interfractional uncertainties," *Journal Name*

[41] J. Y. Chang, H. Li, X. R. Zhu, Z. Liao, L. Zhao, A. Liu, Y. Li, N. Sahoo, F. Poenisch, D. R. Gomez, R. Wu, M. Gillin, and X. Zhang, "Clinical Implementation of Intensity Modulated Proton Therapy for Thoracic Malignancies," *Journal Name*.

[42] E. Sterpin, L. Widesott, K. Poels, M. Hoogeman, E.W. Korevaar, M. Lowe, S. Molinelli, and F. Fracchiolla, "Robustness evaluation of pencil beam scanning proton therapy treatment planning: A systematic review," *Radiotherapy and Oncology*

[43] International Commission on Radiation Units and Measurements. *ICRU Report 83: Prescribing, Recording, and Reporting Photon-Beam Intensity-Modulated Radiation Therapy (IMRT)*. Journal of the ICRU, Volume 10, Issue 1, 2010.

[44] G. J. Kutcher and C. Burman, "Calculation of complication probability factors for non-uniform normal tissue irradiation: The effective volume method," *International Journal of Radiation Oncology, Biology, Physics*, vol. 16, no. 6, pp. 1623-1630, June 1989. doi: 10.1016/0360-3016(89)90936-2

[45] Rodrigues G., Lock M., D'Souza D., Yu E., Van Dyk J., Prediction of radiation pneumonitis by dose-volume histogram parameters in lung cancer: a systematic review, *Radiotherapy and Oncology*, vol. 71, pp. 127-138, 2004.

[46] Willner J., Jost A., Baier K., Flentje M., A little to a lot or a lot to a little? An analysis of pneumonitis risk from dose-volume histogram parameters of the lung in patients with lung cancer treated with 3D conformal radiotherapy, *Strahlentherapie und Onkologie*, vol. 179, pp. 548–559, 2003.

[47] Ricardi U., Filippi A. R., Guarneri A., Giglioli F. R., Mantovani C., Fiandra C., Anglesio S., Ragona R., Dosimetric predictors of radiation-induced lung injury in stere

[48] Stam B., van der Bijl E., Peulen H., Rossi M. M. G., Belderbos J. S. A., Sonke J. J., Dose–effect analysis of radiation-induced rib fractures after thoracic SBRT, *Department of Radiation Oncology, Netherlands Cancer Institute, Amsterdam, The Netherlands.*

Acknowledgements

First and foremost, I would like to express my sincere gratitude to my supervisor, Professor Laura De Nardo, for her unwavering kindness, attention, and support throughout the development of this thesis. I am also deeply grateful to my external advisor at CNAO, Dr. Luca Trombetta, for his availability and the time he generously dedicated to me. I also wish to thank the entire CNAO team I had the opportunity to interact with for their warm welcome, and among them, in particular, Dr. Giuseppe Magro. Moreover, at the conclusion of this journey, which has been not only a path of study, but also one of profound personal growth, I would like to thank all the professors I had the pleasure of learning from.